

Proper orthogonal decomposition reconstruction of a transitional boundary layer with and without control

Hasan Gunes^{a)}

Department of Mechanical Engineering, Istanbul Technical University, Gumussuyu, 80191 Istanbul, Turkey

Ulrich Rist^{b)}

Institut für Aerodynamik und Gasdynamik, Universität Stuttgart, Pfaffenwaldring 21, D-70550 Stuttgart, Germany

(Received 21 October 2003; accepted 6 April 2004; published online 9 June 2004)

Proper orthogonal decomposition (POD) has been performed for controlled and uncontrolled transitional boundary layer data in an effort to reconstruct and possibly control the transitional boundary layer. Although the POD provides mathematically defined optimal basis functions for a given flow, they are only optimal for a given flow condition (e.g., specific Reynolds number, boundary conditions, etc.). In the context of flow control, one is usually forced to use the POD modes extracted from an uncontrolled flow as the controlled flow is not known *a priori*. The present investigation reveals that the most energetic POD modes for uncontrolled and controlled modes show a striking similarity, and unlike in turbulent flows, the present transitional boundary layer flow can be reliably captured by a few POD modes which contain almost all of the flow energy. It is then shown that it is possible to reconstruct the *controlled* flow using POD modes from the *uncontrolled* flow. Therefore, it can be conjectured that low-dimensional models based on the uncontrolled POD modes may be successfully used as online control tools. After this it is shown that “new” snapshots, i.e., the time evolution of the flow, can also be reconstructed by appropriately modifying the coefficients of the POD modes extracted from “previous” or earlier snapshots. This is accomplished using flow-field information at some “sensor positions” and a least-squares fit to the uncontrolled POD modes from former snapshots at these points. The approach introduced in this paper offers a simple, experimentally realizable approach to calculate the temporal coefficients, hence to reconstruct the unknown flow field without the need for a low-dimensional model based on the projection of the Navier–Stokes equations. © 2004 American Institute of Physics.

[DOI: 10.1063/1.1758151]

I. INTRODUCTION

For the past several decades, proper orthogonal decomposition (POD) has been extensively applied to analysis of flow and heat transfer as well as the construction of low-dimensional models (a system of nonlinear ordinary differential equations). We refer to Refs. 1–7, and references therein for the POD procedure and issues in low-dimensional model construction. The general findings compiled from the literature are that the low-dimensional models based on the POD can exactly reproduce the direct numerical simulation (DNS) results on design conditions, i.e., for the parameters that DNS is obtained, while for off-design conditions, low-dimensional models, in general, can only be used to predict DNS results qualitatively.

For the past few years, a new research trend has been to investigate the possibility of using these low-dimensional models as predictors in several control schemes.^{8–12} We shall also mention here that, for cases where an appropriate model

is not known or available and hence construction of a low-dimensional model is not possible, the POD expansion of the ensemble of DNS results can be used to control certain processes. In this regard, Ly and Tran¹³ demonstrated the effectiveness of using the POD to control the temperature distribution inside a Rayleigh–Benard convection cavity without utilization of a mathematical model. They considered two boundary control problems, a temperature tracking problem and a problem that avoids hot spots in a certain region of the domain.

Unlike the computationally expensive control strategies based on the Navier–Stokes equations, the low dimensional models for many complex flows are in general simple enough to offer real-time control capabilities. Ravindran⁸ applied the reduced-order model for optimal control of flow over a backward-facing step and Gerhard *et al.*¹² employed the low-dimensional Galerkin models to active control of laminar vortex shedding behind a circular cylinder, for instance.

Since the controlled flow is not known *a priori*, the low-dimensional models are in general constructed based on the uncontrolled POD basis functions (modes) by assuming that the POD modes do not change appreciably for the controlled and uncontrolled modes. In this way, we accept the fact that

^{a)}Telephone: +90 212 293 1300; fax: +90 212 245 0795; electronic mail: guneshasa@itu.edu.tr.

^{b)}Telephone: +49 711 685 3432; fax: +49 711 685 3438; electronic mail: rist@iag.uni-stuttgart.de

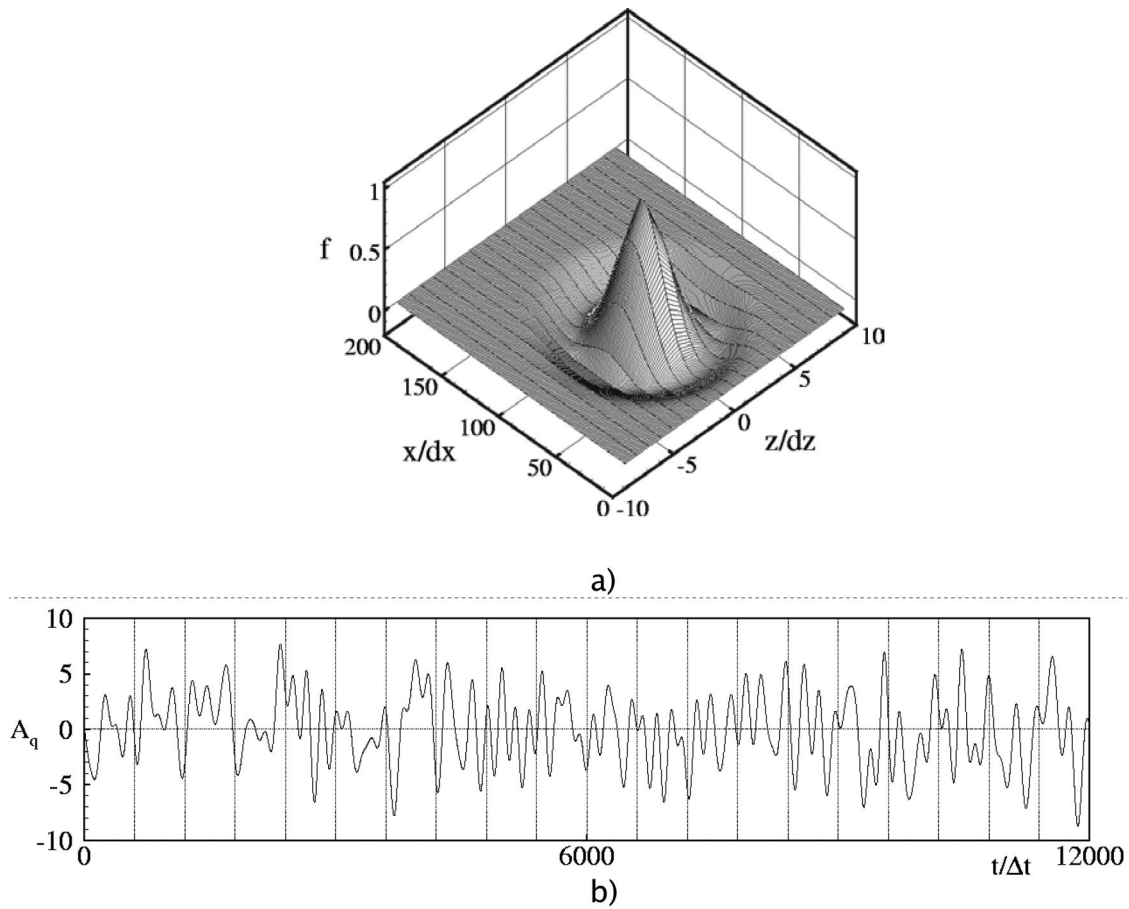


FIG. 1. Illustration of the disturbance source [see Eq. (6)]. (a) Instantaneous wall-normal velocity of the disturbance generator, (b) time signal used to generate nonperiodic point-source disturbances.

the representation of the controlled flow by the uncontrolled POD modes is not optimal as the flow is modified by the control action, e.g., suction/blowing on the boundary. Therefore, before developing low-dimensional models based on the uncontrolled POD modes, one has to make certain for a given problem whether or not the uncontrolled POD modes can be used for flow control.

The influence of control on proper orthogonal decomposition of wall-bounded turbulent flows has been investigated recently by Prabhu *et al.*¹⁴ They have explored the effects of two distinct control strategies (opposition control and opti-

mal control) on the POD basis functions. They conclude that “for flows that employ less effective control strategies (such as opposition control), a low-dimensional model based on the no-control POD basis may perform adequately for a small number of modes although model errors increase with increasing number of modes.” They also stated that it is necessary to manipulate the uncontrolled POD modes to include the effects of the control.

In this paper, we investigate the impact of control on POD modes in the context of a transitional boundary layer and the possibility of controlling transition via a low-

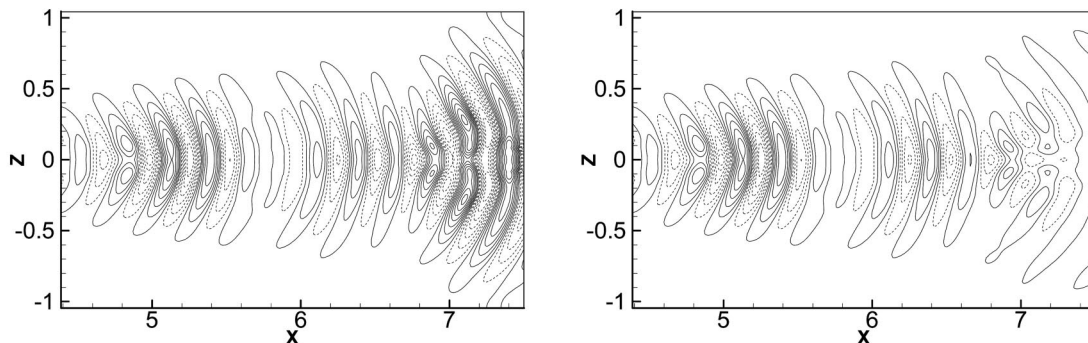


FIG. 2. Instantaneous isocontours of wall vorticity component $\omega_z = \partial u / \partial y - \partial v / \partial x$ at $t/\Delta t = 15120$; (left) uncontrolled case; (right) controlled case.

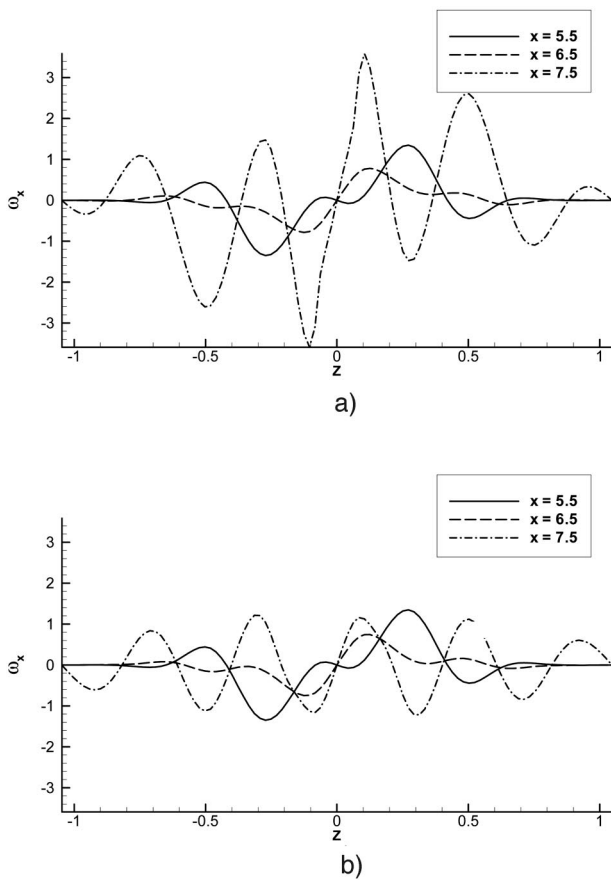


FIG. 3. Spanwise variation of ω_x at the wall ($y=0$) for various cross flow sections: (a) uncontrolled case, (b) controlled case.

dimensional model. In addition, we introduce an experimentally realizable approach to reconstruct the time evolution of the flow. This paper is organized as follows: Section II will contain a review of proper orthogonal decomposition and some of the important properties of the POD modes and coefficients in the context of a transitional boundary layer. In Sec. III, the numerical method for the generation of DNS data and the control mechanism used to actively damp disturbances in boundary layers via feedback of instantaneous signals of spanwise vorticity fluctuations will be outlined. In addition, we will present related DNS data in this section. In Sec. IV we present spatial and temporal results of POD analysis for uncontrolled and controlled cases in a comparative way. In addition, we evaluate the performance of *uncon-*

trolled as well as controlled POD modes in reconstructing the controlled flow for selected number of POD modes. In Sec. V we investigate the possibility of construction of “new” snapshots of the flow field by employing the POD modes that are extracted from “previous” or “earlier” snapshots. Finally, in Sec. VI we summarize our results and make projections for future strategies of realizing the integration of simulation and the experiment for flow prediction.

II. REVIEW OF PROPER ORTHOGONAL DECOMPOSITION

Proper orthogonal decomposition introduced by Lumley¹ has long been popular as a means of extracting the most energetic eigenfunctions (structures) from a flow (or temperature) field data. It has been proved mathematically by Sirovich⁴ that POD eigenfunctions are optimal in terms of kinetic energy of the flow compared to any other basis. The POD eigenfunctions also capture the essential dynamics of the flow and provide insight into the nature of the flow and its instabilities. The implementation of the POD procedure is based on the method of snapshots developed by Sirovich.⁴ Here, we briefly outline the procedure for completeness of the paper. For a detailed treatment of the subject, the reader is referred to the book by Holmes *et al.*² and Refs. 3–7, and 15–18.

Given M instantaneous realizations or “snapshots” of the fluctuating streamwise vorticity as obtained by the DNS, $\omega_x(y, z, t_k)$, corresponding to k different instants in time. For given snapshot data, an optimal basis specific for the field data can be obtained by means of the eigenvectors and eigenvalues of the discrete correlation matrix as defined by,

$$C_{i,j} = \frac{1}{M} \sum_{k=1}^K \sum_{l=1}^L \omega_x(y_k, z_l, t_i) \omega_x(y_k, z_l, t_j). \quad (1)$$

Note that K and L are the number of grid points in the wall normal y and spanwise directions z , respectively. In our simulations we have taken $K=201$ and $L=101$. The advantage of the snapshot version as proposed by Sirovich⁴ is that the order of the correlation matrix is independent of the spatial resolution of the flow field, which enables us to use high resolution data. Here we would also like to mention that we have performed a full three-dimensional (3-D) POD procedure on the 3-D data field for the domain $4.4 < x < 7.5$,

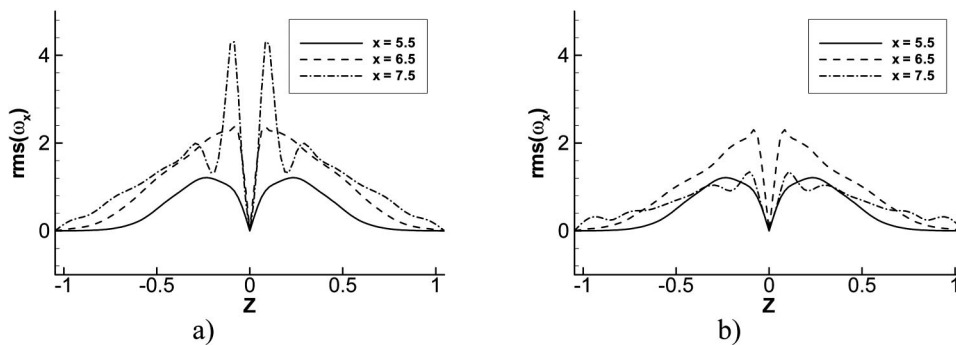


FIG. 4. Spanwise variation of rms value of ω_x at the wall ($y=0$) for various cross flow sections: (a) uncontrolled case, (b) controlled case.

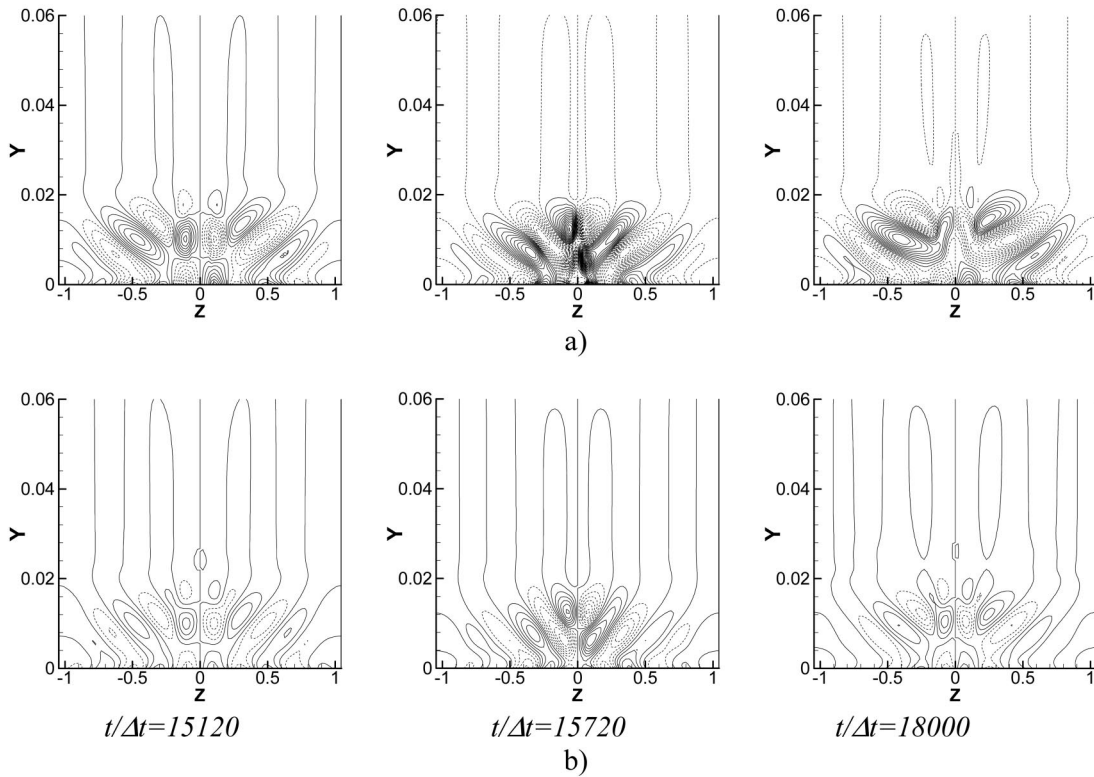


FIG. 5. Snapshots of the instantaneous streamwise vorticity (ω_x) at $x=7.5$: (a) uncontrolled case, (b) controlled case.

$0 < y < 0.13$, $-1.04 \leq z \leq 1.04$ (cf. Sec. III). Although our DNS results are based on 710 grid points in x direction we have used only 298 grid points in the calculation of the correlation matrix. We will present only the two-dimensional (2-D) data due to space considerations but note that similar conclusions are reached by either 2-D or 3-D POD analysis.

Using the (elements of) eigenvectors $\alpha_{k,i}$ of matrix **C** POD eigenfunctions that are optimal for the representation of the corresponding DNS data can be constructed by linearly combining the fluctuating streamwise vorticity as

$$\Psi_k(y, z) = \sum_{i=1}^M \alpha_{k,i} \omega_x(y, z, t_i). \tag{2}$$

The eigenvalues of matrix **C** and the POD basis functions have the following important properties.

(i) POD basis functions (or modes) are orthogonal and after normalization form orthonormal bases, i.e., $(\psi_i, \psi_j) = \delta_{ij}$, where δ_{ij} is the Kronecker symbol and (\cdot, \cdot) denotes the scalar product given as

$$(\Psi_i, \Psi_j) = \int_{\Omega} \Psi_i \Psi_j d\Omega, \tag{3}$$

Ω is the domain of snapshots.

(ii) Eigenvalues are positive ($\lambda_k \geq 0$) and are ordered ($\lambda_k > \lambda_{k+1}$), $k = 1, 2, \dots, M$.

(iii) Each eigenvalue λ_k is associated with the corresponding basis function ψ_k and quantifies the kinetic energy of the flow field (data set). Average fluctuating energy in the data set is represented by summing all of the eigenvalues, $\sum_{k=1}^M \lambda_k = E$.

(iv) POD basis functions can be used to reconstruct the data set optimally for a given number of terms N as follows:

$$\omega_x(y, z, t) \cong \sum_{k=1}^N a_k(t) \Psi_k(y, z). \tag{4}$$

In general (with the possible exception of turbulent flows), the first few modes ψ_k capture most of the energy of the flow as quantified by the normalized values of the λ_k . In other words, in general $N \ll M$.

Equation (4) is usually called the “reconstruction formula” and temporal coefficients $a_k(t)$ can be obtained from Eq. (4) by a “direct projection” formula as

$$a_k(t) = \int_{\Omega} \omega_x(y, z, t) \Psi_k(y, z) d\Omega, \quad k = 1, 2, \dots, N. \tag{5}$$

(v) Another important feature of ψ_k is that because of their construction formula [Eq. (2)], they inherit all properties of the data set. For example, if the flow is incompressible the POD modes are also incompressible. In addition, if

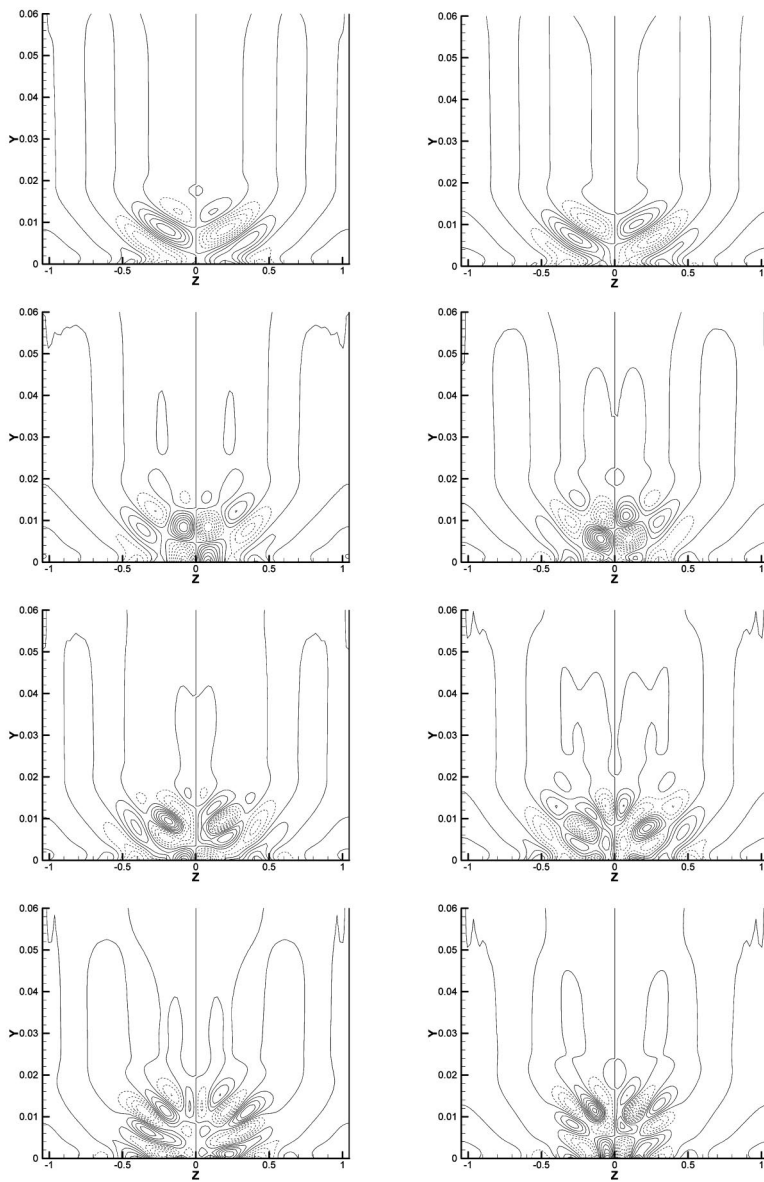


FIG. 6. The first eight most energetic POD modes of the instantaneous streamwise vorticity (ω_x) at $x=5.5$ (uncontrolled case).

boundary conditions of the flow are homogeneous, then these boundary conditions are satisfied by all the POD modes individually.

The above features of POD make it very attractive to derive low-dimensional models for flow control. Substituting Eq. (4) into the full model (usually Navier–Stokes equations), applying the Galerkin method, and making use of the above-mentioned properties of POD modes, a low-dimensional model can be obtained for the expansion coefficients $a_k(t)$.

However, as pointed out by Prabhu *et al.*¹⁴ a limitation of POD basis functions is that they are “intrinsic to the flow” at particular values of parameters or conditions. If one of the flow conditions changes (e.g., change of Reynolds number, or change of boundary conditions), then the POD modes will also change. For example, the controlled flow field used in this paper has been obtained by employing so-called ω_z control. According to this control strategy, the spanwise vorticity fluctuations at the wall are sensed and, after a suitable

amplification, prescribed as a new v -boundary condition at the wall to damp the disturbance in the boundary layer.¹⁹ Therefore, strictly speaking, the POD modes for the ω_z -controlled flow will not be the same as the uncontrolled POD modes. Hence, for an optimal representation of the controlled flow one should actually use the controlled POD basis. However, one is usually forced to construct a low-dimensional model based on the uncontrolled POD modes in an effort to control a flow because the controlled POD basis is not known *a priori*. Then, one would like to have an answer to the question “can uncontrolled POD modes be used in a low-dimensional model to describe the dynamics of the controlled flow?” It is expected that the answer will depend on the type of control, i.e., how strong the uncontrolled flow is changed and the complexity of dynamics of the flow. As a preliminary condition of constructing a valid low-dimensional model, one has to include enough energy (typically over 90%) of the flow field as quantified by the

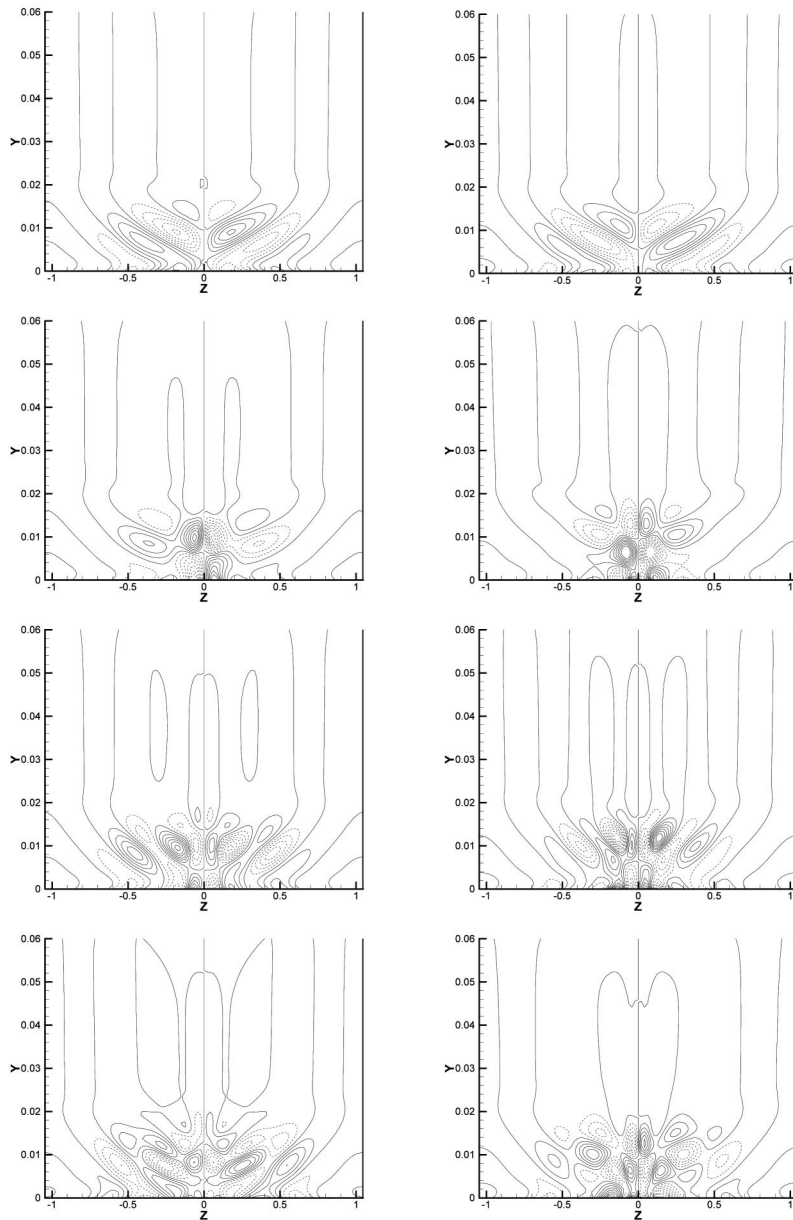


FIG. 7. The first eight most energetic POD modes of the instantaneous streamwise vorticity (ω_x) at $x=6.5$ (uncontrolled case).

eigenvalues of the correlation matrix. Turbulent flows have a very low rate of converge of energy as reflected by the eigenvalue spectrums. For example, Prabhu *et al.*¹⁴ report that for the turbulent channel flow (both controlled and uncontrolled cases) over 500 POD eigenfunctions are required to account for approximately 65% of the total flow energy. With such low energy content, even the reconstruction of the turbulent flow dynamics may not be possible and the size of the models certainly limits their use for real-time control applications. On the other hand, for transitional flows, most of the flow energy is captured by a few (most energetic, usually less than 20) modes, and therefore the reconstruction, cross projection, and projection of the “future” flow dynamics (employing POD modes to capture a flow for different conditions) may be possible. This will be shown later.

III. GENERATION OF SNAPSHOT DATA

A. Numerical method

The DNS data used for the present investigation have been obtained from a continuation of the work by Gmelin *et al.*,^{19,20} which is described in more detail in Gmelin.²¹ The numerical method used is based on the vorticity–velocity formulation of the Navier–Stokes equations for incompressible fluids. A two-dimensional flat-plate (Blasius) boundary layer from $Re^* = U_\infty \delta^* / \nu = 1.72077 \sqrt{Re x} = 912$ to $Re^* = 1640$ (δ^* = displacement thickness and $Re = 100\,000$) is taken as base flow for investigating the unsteady three-dimensional reaction of the flow to random forcing through a hole in the flat plate. The scenario is similar to the wind-tunnel experiments of Shaikh.²²

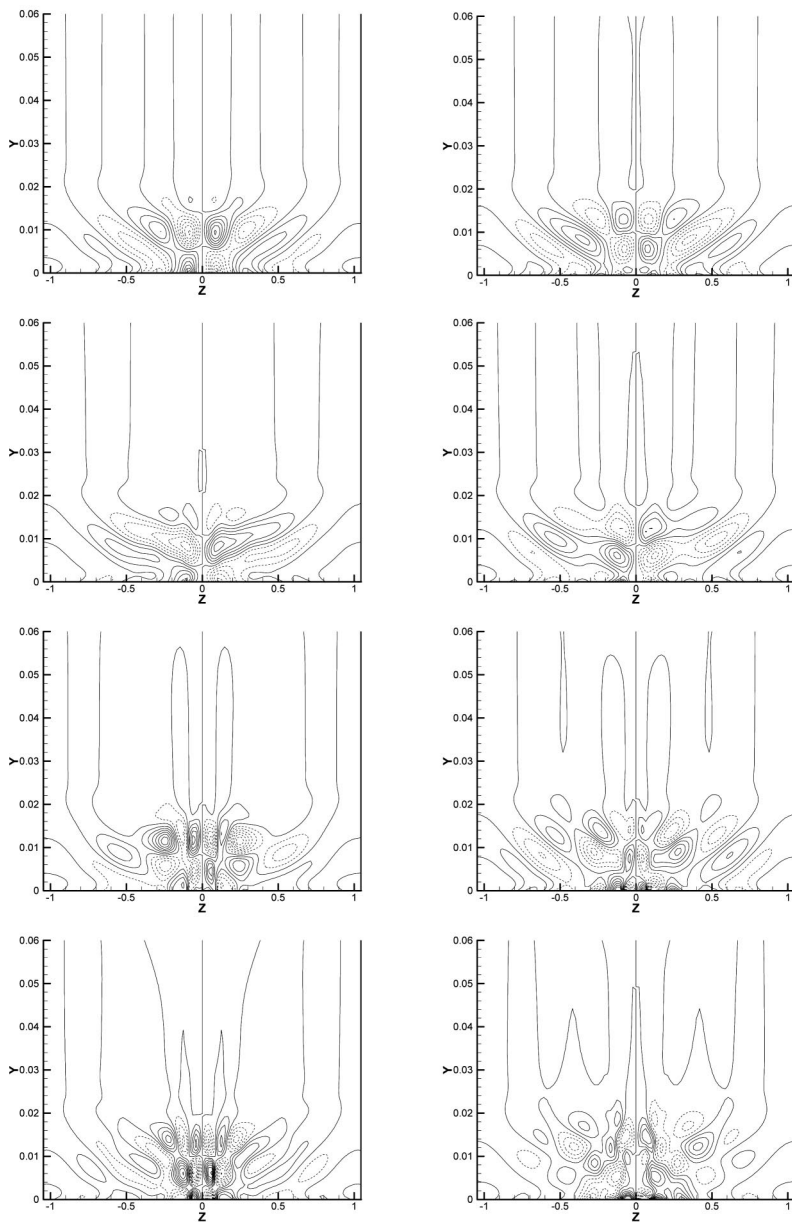


FIG. 8. The first eight most energetic POD modes of the instantaneous streamwise vorticity (ω_x) at $x=7.5$ (uncontrolled case).

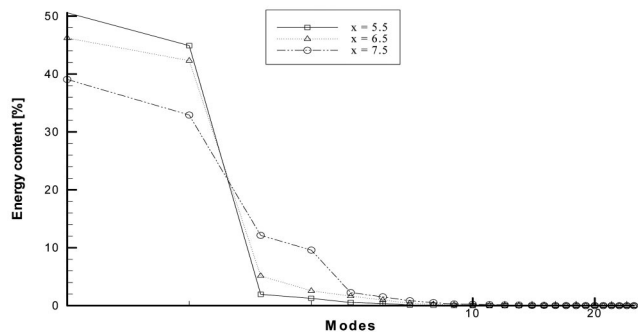
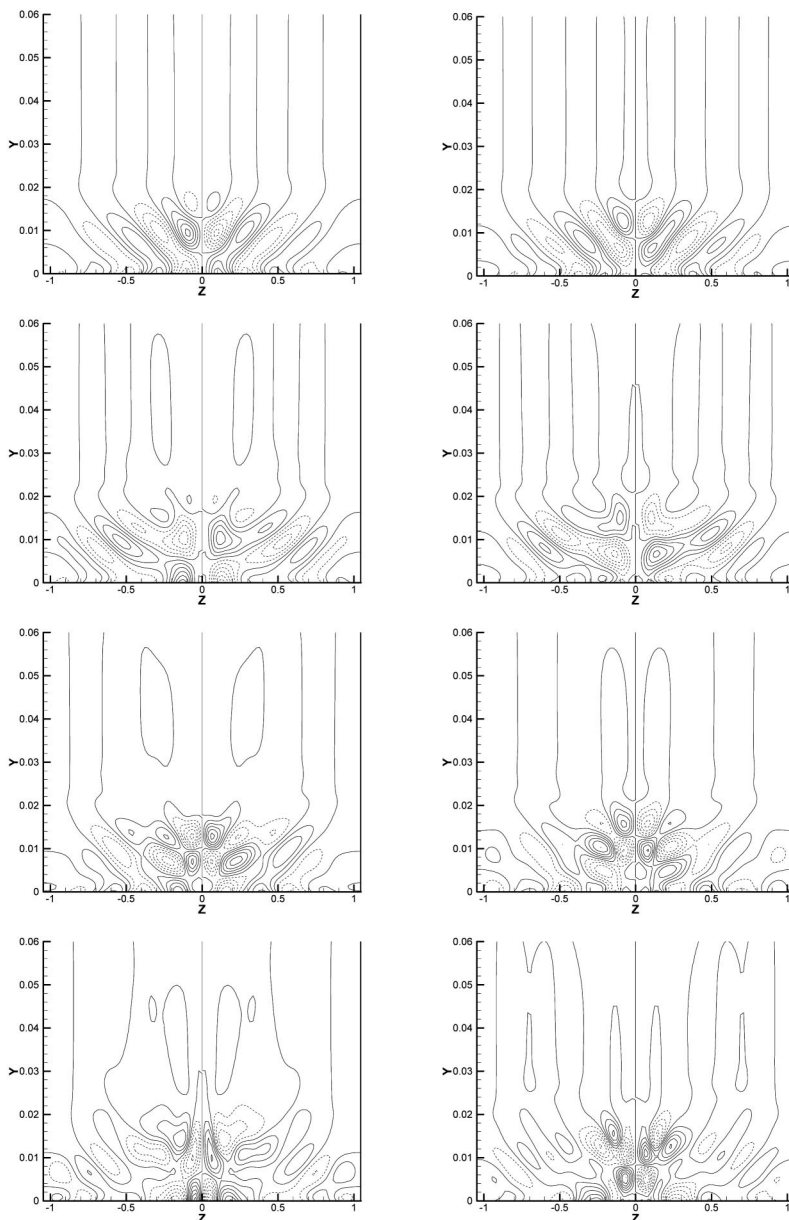


FIG. 9. Energy content of each POD mode for uncontrolled case at selected cross-flow sections.

Discretization of the governing equations is performed by a Fourier transform in spanwise (z -) direction followed by standard fourth-order-accurate central finite differences in streamwise (x) and wall normal directions (y), as described in Rist and Fasel,²³ except for the x -convection terms which are discretized by one-sided finite differences which exhibit fourth-order accuracy when applied in an alternating up- and downwind manner.²⁴ The initial conditions for the simulations are zero disturbances throughout the integration domain. Disturbances are introduced through suction and blowing at the wall as described later. At the inflow boundary which is placed one typical disturbance wavelength upstream of the suction and blowing hole, zero disturbances are assumed for all time. At the free-stream boundary the vorticity

TABLE I. Normalized eigenvalues and their cumulative contribution to the fluctuating energy.

	$x=5.5$		$x=6.5$		$x=7.5$		$x=7.5$ (controlled)	
	λ_j	$\Sigma\lambda_j$	λ_j	$\Sigma\lambda_j$	λ_j	$\Sigma\lambda_j$	λ_j	$\Sigma\lambda_j$
1	50.59	50.59	46.23	46.23	39.06	39.06	47.22	47.22
2	44.91	95.50	42.31	88.54	32.92	71.98	42.45	89.67
3	1.96	97.46	5.14	93.68	12.14	84.12	3.56	93.23
4	1.27	98.73	2.56	96.24	9.59	93.71	3.12	96.35
5	0.56	99.29	1.65	97.89	2.26	95.97	1.16	97.51
6	0.38	99.67	0.98	98.87	1.52	97.49	0.84	98.35
7	0.13	99.80	0.42	99.29	0.85	98.34	0.55	98.90
8	0.08	99.88	0.25	99.54	0.52	98.86	0.42	99.32
9	0.03	99.91	0.14	99.68	0.29	99.15	0.23	99.55
10	0.02	99.93	0.14	99.82	0.23	99.38	0.20	99.75

FIG. 10. The first eight most energetic POD modes of the instantaneous streamwise vorticity (ω_x) at $x=7.5$ (controlled case).

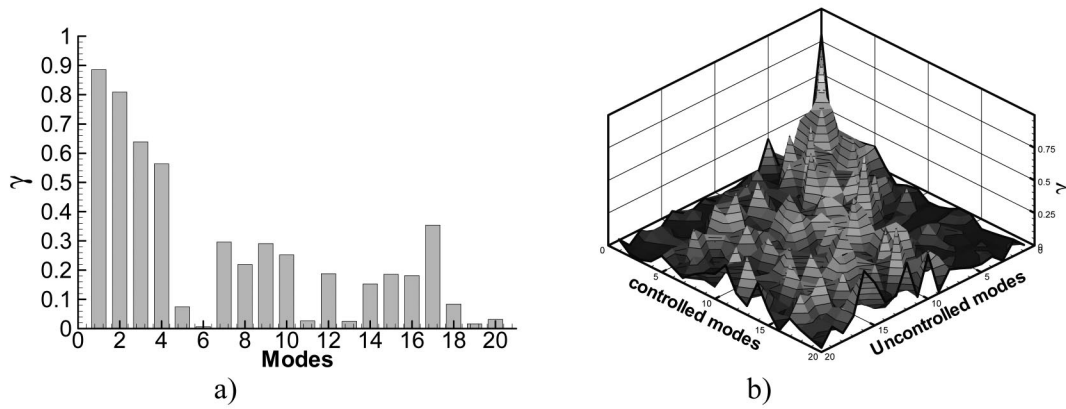


FIG. 11. Comparison of POD modes of the uncontrolled and controlled cases: (a) γ_{ii} , $i = 1, 2, \dots, N$, (b) γ_{ij} , $i, j = 1, 2, \dots, N$.

is zero and the velocity decays exponentially for $y \rightarrow \infty$. The “relaminarization zone” by Kloker *et al.*,²⁵ which reduces the disturbance vorticity to zero, is applied upstream of the end of the integration domain. The vorticity at the wall is computed from the conditions specified in Kloker *et al.*²⁵ and Rist and Fasel²³ which take into account the zero divergence of the velocity and the vorticity vectors. Based on the solution of the previous time step the nonlinear convection terms in the discretized vorticity-transport equations (one for every component of the three-dimensional vorticity vector) are computed using the pseudospectral technique. Time integration is then performed applying the standard fourth-order-accurate four-step Runge–Kutta scheme.

The instantaneous wall-normal velocity component at the wall used as a zero-net-mass-flux disturbance generator is depicted in Fig. 1(a) together with the computer generated “white noise” time signal of the forcing amplitude in Fig. 1(b). The velocity is defined by

$$v(x, y=0, z, t) = A_v A_q(t) f(x, z), \tag{6}$$

$$f = \left(\left(\left(14 \frac{r}{R} - 45 \right) \frac{r}{R} + 50 \right) \frac{r}{R} - 20 \right) \left(\frac{r}{R} \right)^2 + 1,$$

where r and R are the radius of the point source and the distance to the center of the point source, respectively. For the present investigations $R = 0.314$ and $A_v = 2 \times 10^{-4}$ have been chosen and the center of the disturbance source was placed at $Re^* = 974$ ($x = 3.2$). The time series $A_q(t)$ was generated using computer generated random phases and a constant amplitude for all frequencies $0.3 \leq \beta \leq 24$, where $\beta = 2\pi f$.

The computations have been run with 200 equidistant intervals in wall-normal direction (for $15\delta^*$ at the inflow boundary) and different stream- and spanwise resolutions, e.g., 2402 and 3202 grid points in x and 50, respectively, 100 conjugate complex fully de-aliased Fourier modes in span. Thus, for the coarsest of these simulations, the step sizes correspond to $\Delta x = 0.002618$, $\Delta y = 0.0006847$, and $\Delta z = 0.02094$ (normalized with a reference length $L = 5$ cm for $U_\infty = 30$ m/s). Time was discretized with $\Delta t = 0.001745$ in both cases.

Since the objective of Gmelin²¹ was to contribute to laminar-turbulent transition control, a control strip was placed in the simulations between $x = 6.16$ and $x = 8.26$, where an extension of the feedback algorithm already described in Gmelin *et al.*¹⁹ has been applied. This algorithm senses the instantaneous wall vorticity component $\omega_z = \partial u / \partial y - \partial v / \partial x$ and prescribes it as wall-normal velocity controlled by a FIR filter. In spectral space the control algorithm reads

$$V(x, y=0, \alpha, k) = |A(x)| H(\alpha) \Omega_z(x, y=0, k), \tag{7}$$

where capital letters for V and Ω_z denote the spectral amplitudes of the respective velocity or vorticity components with respect to the spanwise Fourier ansatz (index k), α is a streamwise wave number, and $H(\alpha)$ the complex filter vector of the FIR filter. The feedback gain $A(x)$ provides user control and a smooth ramping of the control at the up- and downstream ends of the control strip. Amplitude and phase of $H(\alpha)$ were adjusted in such a way as to provide nearly optimal damping for every spanwise Fourier mode covering the whole region of linear instability. More details are given in Gmelin.²¹

B. DNS results

From the simulation runs the full vorticity and velocity fields have been stored at every 120th time step in the region $4.38 < x < 8.10$ at every second grid point in x . For conver-

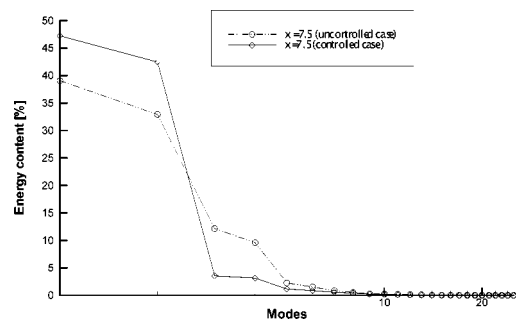


FIG. 12. Energy content of POD modes for controlled and uncontrolled cases.

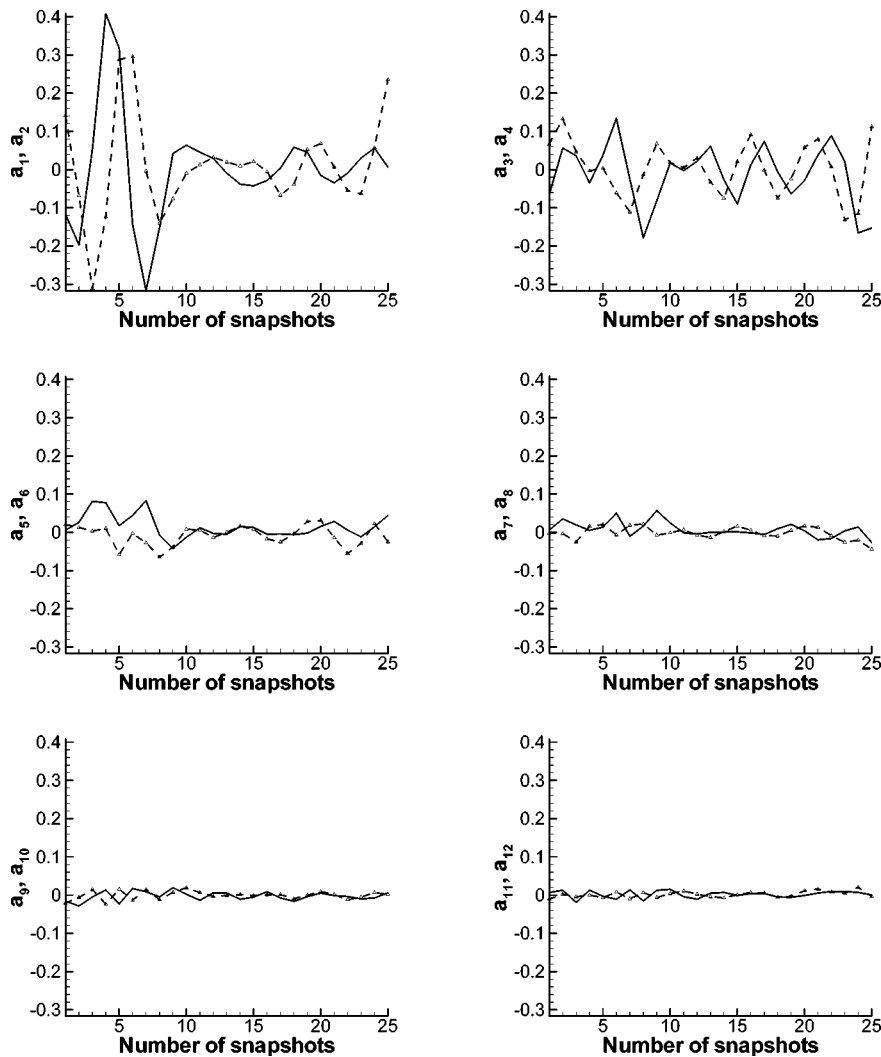


FIG. 13. Temporal coefficients of POD modes for uncontrolled case at $x=7.5$. Solid lines denote the odd coefficients, dashed lines denote the even coefficients.

gence checks of the PODs the z component of the wall vorticity was available at full spatial and increased temporal resolution, as well. For the following investigations the uncontrolled case and a controlled case with $\max\{A(x)\}=3 \times 10^{-4}$ for Fourier modes $0 \leq k \leq 9$ have been chosen.

A depiction of the downstream disturbance development induced by the forcing given by Eq. (6) and illustrated in Fig. 1 is shown in Fig. 2 comparing instantaneous isocontours of disturbance wall vorticity component ω_z for the uncontrolled and the controlled case.

The forcing at $x=3.2$ produces a series of wave packets similar to those observed by Shaikh.²² The disturbance amplitude A_v has been chosen such that the first nonlinear structures (Λ vortices) develop for $x > 6.0$. Final transition happens around $x=8.0$ with a certain intermittency that depends on the characteristics of the particular wave packet (e.g., its amplitude, spectral content, and phase). Upstream of the control strip (i.e., for $x < 6.2$) the two realizations in Fig. 2 are identical, as expected. But inside the control strip the effect of the feedback control becomes apparent, especially toward the downstream end of the region shown. Figures like this indicate that the present control algorithm successfully works in the nonlinear stages of laminar-turbulent transition.

From our 3-D vorticity field, we have extracted two-

dimensional data at selected values of constant x cross sections. One of our motivations to particularly investigate the constant x positions is that we apply control for $x \geq 6.2$. So, by analyzing data for a constant x value larger than 6.2, we are able to compare POD analysis for uncontrolled and controlled flow data. We believe that, in this way, drastic changes in POD modes can be observed best, if they indeed exist. Therefore, we have chosen to present cross sections at $x=5.5$, $x=6.5$, and $x=7.5$. At $x=5.5$, the control has not yet been applied, at $x=6.5$ it has already been applied but does not yet have an appreciable effect, while at $x=7.5$ the effect of control is clearly seen as depicted in Fig. 3. Figure 3 compares the instantaneous spanwise variation of ω_x at the wall ($y=0$) for uncontrolled and controlled cases, while in Fig. 4 the rms values of ω_x are depicted to illustrate the effect of control via

$$\text{rms}[\omega_x(y,z)] = \sqrt{\frac{1}{M} \sum_{i=1}^M \omega_x(y,z,t_i)^2}. \quad (8)$$

It is seen that while the effect of the control is minimal for $x=6.5$, for $x=7.5$ disturbances are greatly reduced to a level comparable with the section $x=5.5$. The success of the ω_z control is also evident in Fig. 5, where typical snapshots of

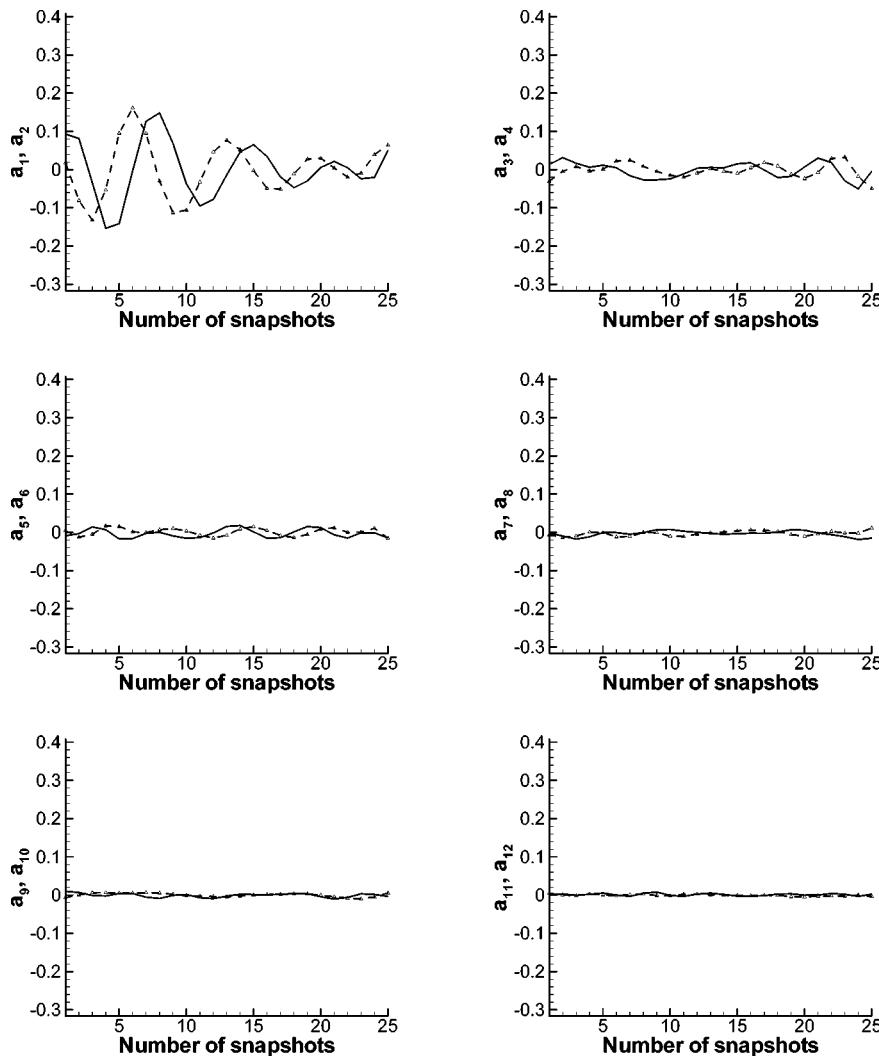


FIG. 14. Temporal coefficients of POD modes for controlled case at $x = 7.5$. Solid lines denote the odd coefficients, dashed lines denote the even coefficients.

the instantaneous streamwise vorticity (ω_x) at the plane $x = 7.5$ are compared for both uncontrolled and controlled cases.

IV. POD RESULTS

A. POD modes for uncontrolled flow

Here, we start by comparing the POD modes in three cross sections for uncontrolled flow. This investigation in a certain sense will enable us to get an understanding of the evolution of characteristic structures (as reflected by POD modes) during transition of the boundary layer. If these modes are found to have a certain similarity, we hope that the flow downstream may be reconstructed by employing the POD basis extracted from upstream. In Figs. 6–8, the first eight most energetic POD modes of the streamwise vorticity are shown for the cross sections $x=5.5$, $x=6.5$, and $x=7.5$, respectively. It is seen that POD modes extracted for $x=5.5$ and $x=6.5$ are very similar to each other, while there are more pronounced differences for $x=7.5$. Figure 9 compares the energy content of each POD mode for uncontrolled flow at the indicated cross sections. It is seen that for all cross sections, eigenvalues occur in pairs of similar magnitude and there is always a large gap between these pairs. This

behavior has been observed in many flows and attributed to traveling waves (see, e.g., Refs. 26 and 27) including transitional boundary-layer flows (Rempfer^{5,17}). Figure 9 also shows that pairing is more pronounced for upstream stations ($x=5.5$), and it diminishes as the transition progresses downstream. For quantitative comparison, we also provide normalized eigenvalues and their cumulative contribution to the fluctuation energy in Table I. As transition progresses downstream, the first pair consisting of the two most energetic modes, loses its energy to the higher-order modes. For example, at $x=5.5$, the first pair captures over 95% of the total energy, while at $x=6.5$ and $x=7.5$, they capture only about 88% and 72%, respectively. Fortunately, the energy lost by the first pair is captured by the next few most energetic pairs, instead of dissipating further. Therefore, in order to capture over 99% of the energy of the flow, only five modes are necessary for section $x=5.5$, while seven modes and nine modes are necessary for sections $x=6.5$ and $x=7.5$, respectively.

B. A comparison with POD modes for controlled flow

We now compare POD results (i.e., POD modes, energy contents, and temporal coefficients) for controlled and un-

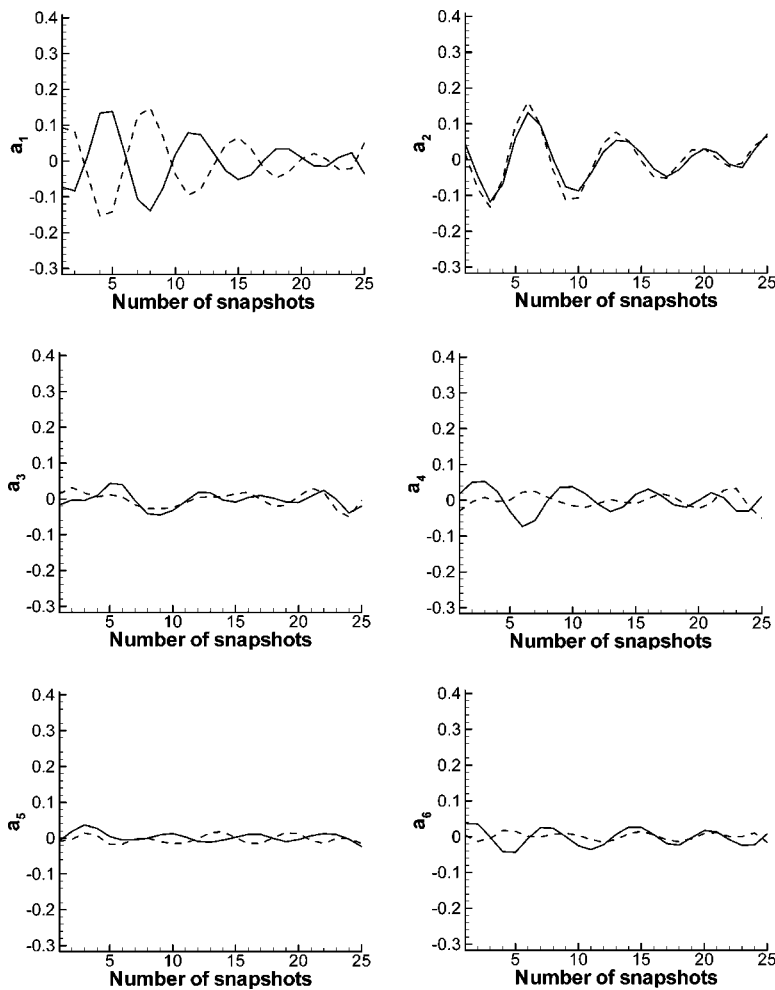


FIG. 15. Temporal reconstruction of controlled flow dynamics via uncontrolled POD modes. Solid lines denote the temporal coefficients computed by cross projection with the no-control model, i.e., a_k^{model} . Dashed lines denote the temporal coefficients computed by the POD of the controlled flow, a_k^{control} . Note: Phase shift between a_1^{model} and a_1^{control} is observed because corresponding spatial POD modes are different in sign. (See Figs. 6 and 8.)

controlled flow. We shall note here that POD results for both controlled and uncontrolled cases at section $x = 6.5$ are almost identical because the effect of the control is not felt for some distance downstream. However, for sufficiently large distance downstream, the effects of the control become very clear (see Figs. 2–5). Therefore, our comparison between controlled and uncontrolled flow is done at section $x = 7.5$. Figure 10 shows the first eight most energetic *controlled* POD modes at the section $x = 7.5$. First of all, by comparing visually Figs. 8 and 10, we see that the most energetic first pair is quite similar for both cases. For higher modes, however, we observe some differences between the POD modes. In order to compare the POD basis (or any two different flow fields) objectively, one has to use a quantitative measure for the similarity or dissimilarity of the structures compared. Therefore, as proposed in Rempfer *et al.*,²⁸ we use the scalar product given in Eq. (3) to define a “similarity number” to indicate the similarity between any POD modes. The similarity number, denoted by the symbol γ_{ij} , is based on the scalar product defined as

$$\gamma = \gamma_{ij} = |(\psi_i^1, \psi_j^2)|, \quad i, j = 1, 2, \dots, N, \quad (9)$$

where superscripts 1 and 2 refer to the uncontrolled and controlled flows, respectively.

In the above definition we use the absolute value in order to eliminate negative values since $\gamma = -1$ denotes that the two compared modes are only different in sign. Therefore, the values of similarity parameter as defined above are in the range $0 \leq \gamma \leq 1$ and $\gamma = 1$ means that two compared modes (structures) are identical to each other. As $\gamma \rightarrow 0$, the compared structures become dissimilar to each other. In addition, in Eq. (9) if $i = j$, then there is a one-to-one comparison between the modes, i.e., the first POD mode of the controlled flow, for example, is compared with the first POD mode of the uncontrolled flow. However, due to possible “mode crossings,” it is possible that the i th POD mode of the controlled flow is similar and needs to be compared with the $(i \pm 1)$ th POD mode of the uncontrolled flow.

Figure 11(a) depicts a one-to-one comparison ($\gamma_{ii}, i = 1, 2, \dots, N$) of the uncontrolled and controlled POD modes at section $x = 7.5$. The first POD modes (the most energetic ones) for the controlled and uncontrolled case resemble each other the most with a similarity number near 0.9 (see also Figs. 8 and 10 for visual comparison). For the first four modes γ decreases gradually, as expected. However, for the fifth and sixth modes we see that γ takes very small values indicating that the fifth and sixth modes are dissimilar. This can also be verified visually by carefully checking the corre-

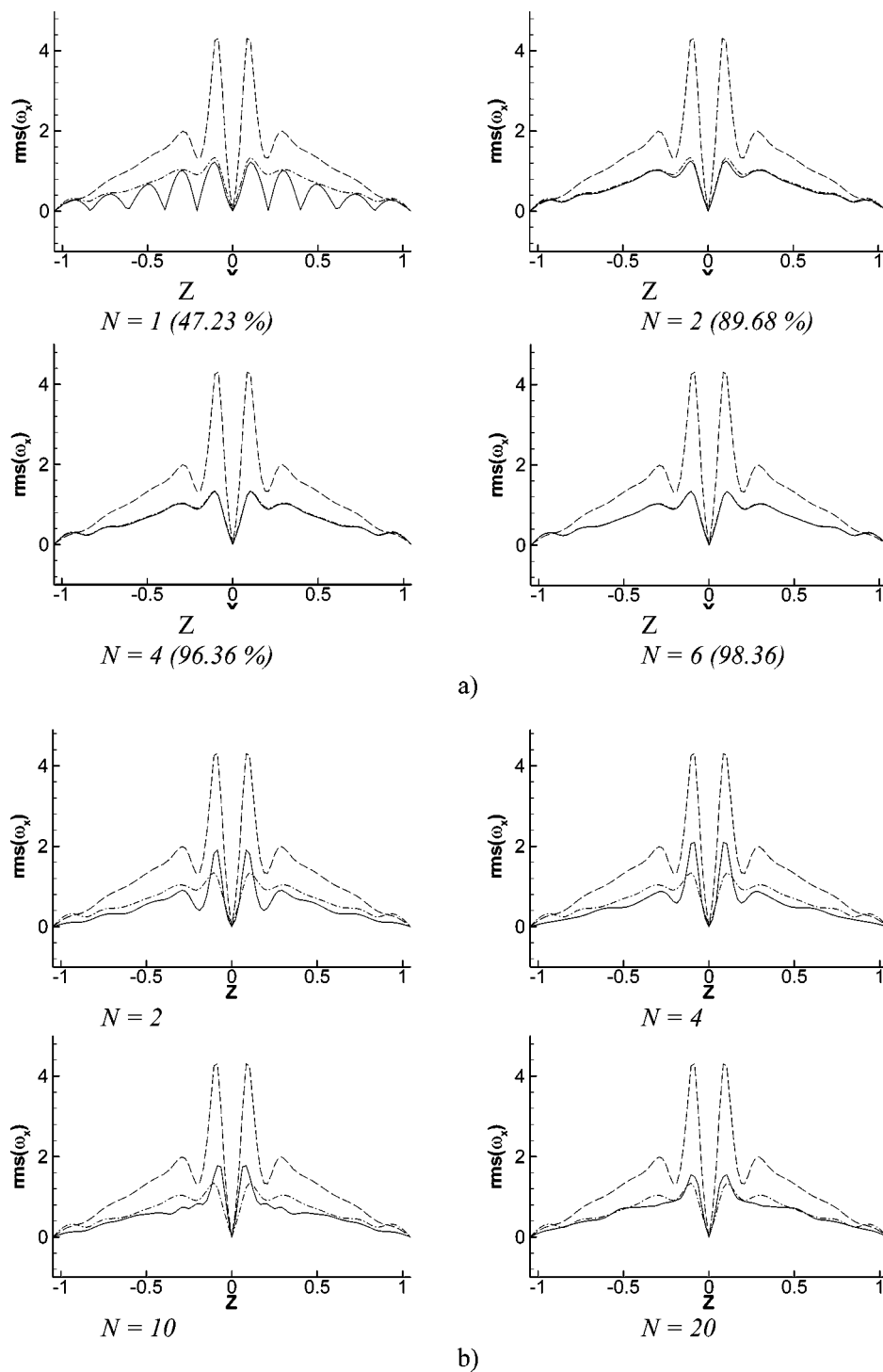


FIG. 16. Controlled flow reconstruction. Spatial variation of rms values of ω_x on the wall for different number of POD basis: (a) Reconstruction via controlled POD modes, (b) reconstruction via uncontrolled POD modes. Solid line: reconstructed data, dashed line: uncontrolled DNS data, dashed-dotted line: controlled DNS data.

sponding modes in Figs. 8 and 10. An explanation for this is the so-called “mode crossing” that occurs with change of sign of the eigenvalues as reported in Rempfer *et al.*²⁸ and Prabhu *et al.*¹⁴ For a detailed discussion of the mode crossings we refer to Prabhu *et al.*¹⁴ The conclusion is that “mode crossing” can occur and one should not be misled by ignoring it. In order to clarify the subject, for example, we note that due to the crossings of the POD modes, the sixth mode of the uncontrolled case is actually similar to the fifth mode of the controlled case ($\gamma_{5,6}=0.554$) and likewise, the fifth

mode of the uncontrolled case is similar to the sixth mode of the controlled case ($\gamma_{6,5}=0.335$).

In Fig. 11(b), we plot the $\gamma_{i,j}$ as a function of all of the most important 20 modes in order to illustrate the mode crossings and the similarities between any two modes. If there was a perfect agreement between the structures of the controlled and uncontrolled cases (with no mode crossings), the similarity number should be exactly 1 along the diagonal and should vanish symmetrically away from the diagonal. However, as can be seen from Fig. 11(b) there are many

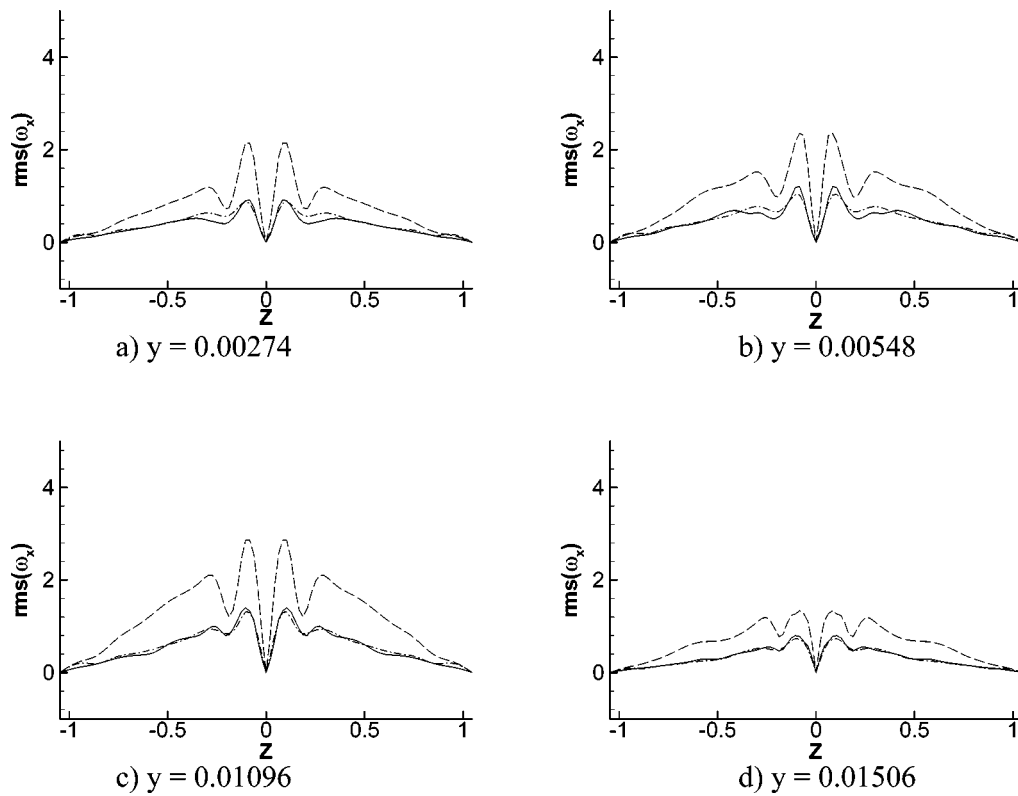


FIG. 17. Reconstruction of spatial rms values of ω_x off the wall for various values of wall normal distances. All reconstructions are based on $N=20$ POD modes. Solid line: reconstruction using *uncontrolled* POD modes, dashed line: controlled DNS data, long dashed line: uncontrolled DNS data.

mode crossings and hence many “off-diagonal similarities.”

Figure 12 shows the energy content of each POD mode for the controlled and uncontrolled cases. We note that the relative contribution of the first mode pair (in percent) to the total fluctuation energy is considerably higher for the controlled case and given a mode number, the cumulative contribution of the energy is always larger for controlled flows (see Table I). This is in agreement with the statement by Prabhu *et al.*¹⁴ that “POD for the controlled flows tends to converge faster than the no control flow.”

C. Reconstructions of controlled flow via POD modes

While the most energetic POD modes (especially the first pair) extracted from the controlled and uncontrolled flow show a remarkable similarity, their temporal coefficients $a_k(t)$ calculated by the direct projection formula [Eq. (5)] show drastic changes as illustrated in Figs. 13 and 14. First of all, we note that the most energetic coefficients [especially the first pair, i.e., $a_1(t)$ and $a_2(t)$] are quite different in both temporal behavior and in magnitude. Let us write the decomposition for controlled and uncontrolled flow cases:

$$\omega_x^{\text{no control}}(y, z, t) \cong \sum_{k=1}^N a_k^{\text{no control}}(t) \Psi_k^{\text{no control}}(y, z), \quad (10)$$

$$\omega_x^{\text{control}}(y, z, t) \cong \sum_{k=1}^N a_k^{\text{control}}(t) \Psi_k^{\text{control}}(y, z). \quad (11)$$

Because the first few modes are quite similar as depicted in Fig. 11, i.e., $\psi_1^{\text{no control}} \cong \psi_1^{\text{control}}$, $\psi_2^{\text{no control}} \cong \psi_2^{\text{control}}$, etc., the different DNS data in Figs. 2–5 can only be obtained by the corresponding large changes in temporal coefficients, i.e., $a_1^{\text{no control}}(t) \neq a_1^{\text{control}}(t)$, etc.

Therefore, we conclude that in our transitional boundary layer flow, it may be possible to use uncontrolled POD modes in order to construct a low-dimensional model for the controlled flow. However, the coefficients for the uncontrolled flow have to be changed, or in other words, by utilizing some of the information from the controlled case (e.g., taking measurements using sensors at selected points) the controlled temporal coefficients have to be obtained. Now let us define model coefficients, a_k^{model} as follows:

$$\omega_x^{\text{control}}(y, z, t) \cong \sum_{k=1}^N a_k^{\text{model}}(t) \Psi_k^{\text{no control}}(y, z), \quad (12)$$

where

$$a_k^{\text{model}}(t) = \int_{\Omega} \omega_x^{\text{control}}(y, z, t) \Psi_k^{\text{no control}}(y, z) d\Omega. \quad (13)$$

In Eq. (13) a_k^{model} will be, of course, different from a_k^{control} given in Eq. (11) since the POD modes are similar but not the same for the controlled and uncontrolled cases.

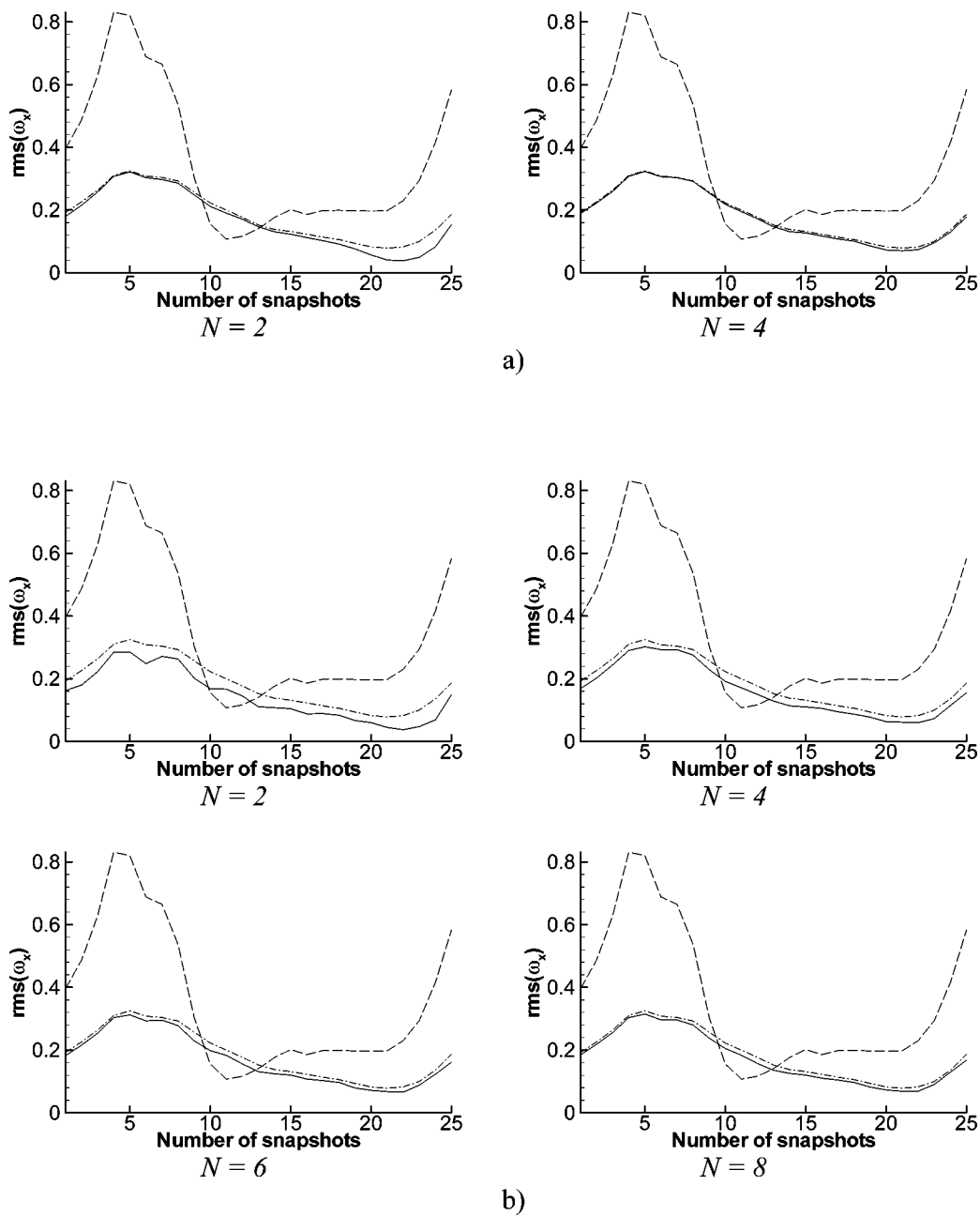


FIG. 18. Controlled flow reconstruction. Temporal rms values of ω_x at $x=7.5$ for different number of POD basis: (a) reconstruction via controlled POD modes, (b) reconstruction via uncontrolled POD modes. Solid line: reconstructed data, dashed line: uncontrolled DNS data, dashed-dotted line: controlled DNS data.

Equation (13) is called the “cross projection” by Prabhu *et al.*¹⁴ and we stick here to their definition. As reported in Ref. 14, the cross projection represents the ability of uncontrolled POD modes to describe the actual controlled flow dynamics. Therefore, by comparing a_k^{model} and a_k^{control} , we can evaluate *a priori* the potential of non-optimal bases to be used as models for controlled flows. Unlike turbulent flows, low-dimensional models constructed for transitional flows have minimal truncation errors as the models can easily be constructed with the first few modes capturing most of the flow energy (about 99%). This feature leaves the cross projection as a crucial check before constructing a low-dimensional model with certain bases. Figure 15 shows the

temporal coefficients of controlled flow dynamics via uncontrolled POD modes. Solid lines denote the temporal coefficients a_k^{model} computed by cross projection with the no-control model using Eq. (13), while dashed lines denote the temporal coefficients a_k^{control} computed by the POD of the controlled flow. A phase shift between a_1^{model} and a_1^{control} is observed because corresponding spatial POD modes differ in sign as can be seen by comparing the first POD modes in Figs. 8 and 10. The comparison is very good for the first pair, which constitutes the most important structures of the flow. For higher modes, some differences in the amplitudes and the phase shift can be observed. Next, reconstructions of

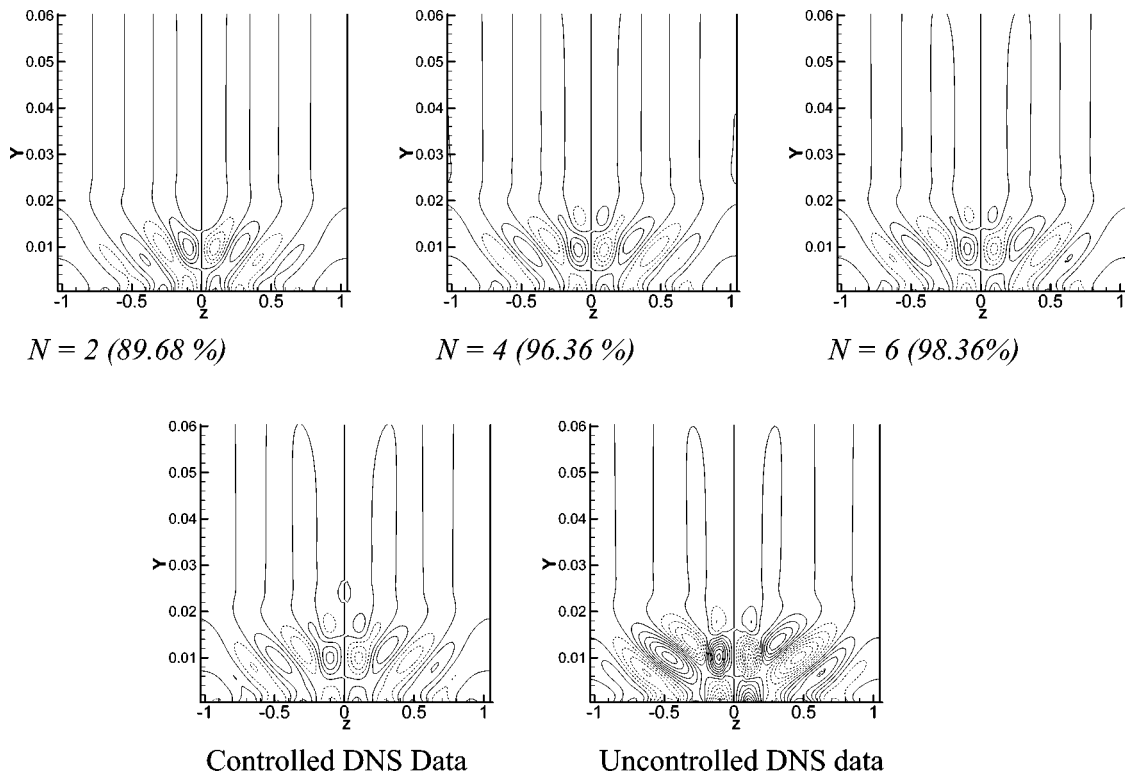


FIG. 19. Reconstruction of instantaneous ω_x of controlled flow at $t/\Delta t = 15\ 120$ via *controlled* POD modes. DNS data are also shown for comparison.

controlled DNS data using both controlled POD modes [Eq. (11)] and uncontrolled POD modes [Eq. (12)] are shown in Fig. 16, where the rms values of ω_x are depicted as defined in Eq. (8) in order to reflect all snapshot data. Figure 16(a) depicts the direct projection reconstruction, i.e., reconstruction via *controlled* POD bases, while Fig. 16(b) shows the cross projection reconstruction, i.e., reconstruction via *uncontrolled* POD bases. In Fig. 16, solid lines denote the re-

constructions obtained by Eq. (11) or Eq. (12) and uncontrolled and controlled DNS data are also shown for comparison. Only the two most energetic modes ($N=2$), which capture almost 90% of the total flow energy, seem to be enough for accurate reconstruction of the flow if one could use the controlled POD modes, which are usually not known *a priori*. Clearly such a low number of uncontrolled POD modes are not capable of reconstructing the controlled flow as can be seen in Fig. 16(b). However, by increasing the number of uncontrolled POD modes, one can reasonably reconstruct the controlled flow. For example, with 20 uncontrolled modes, a reasonable agreement is achieved, especially considering the differences between the two DNS data. Note that in Fig. 16, reconstructions are performed at the wall ($y = 0$), where the control is applied. The flow field as well as the POD bases are mostly different on the wall. Therefore, away from the wall, the ability of uncontrolled POD bases to reconstruct the controlled DNS data is expected to be much better as depicted in Fig. 17, where cross projection reconstructions are given for various values of wall normal distances. Clearly reconstruction improves away from the wall.

In order to compare the temporal behavior of the DNS and the reconstruction data, we define a temporal rms value as

$$\text{rms}[\omega_x(t)] = \sqrt{\frac{1}{K \times L} \sum_{k=1}^K \sum_{l=1}^L \omega_x(y_k, z_l, t)^2}. \quad (14)$$

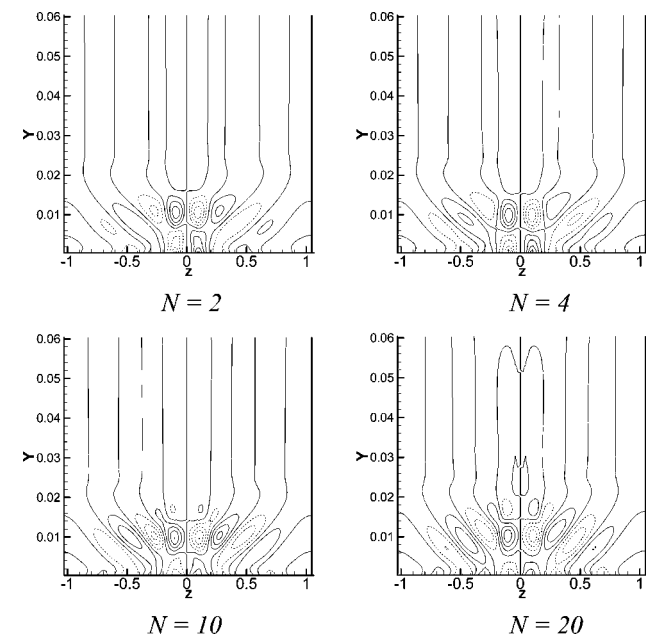
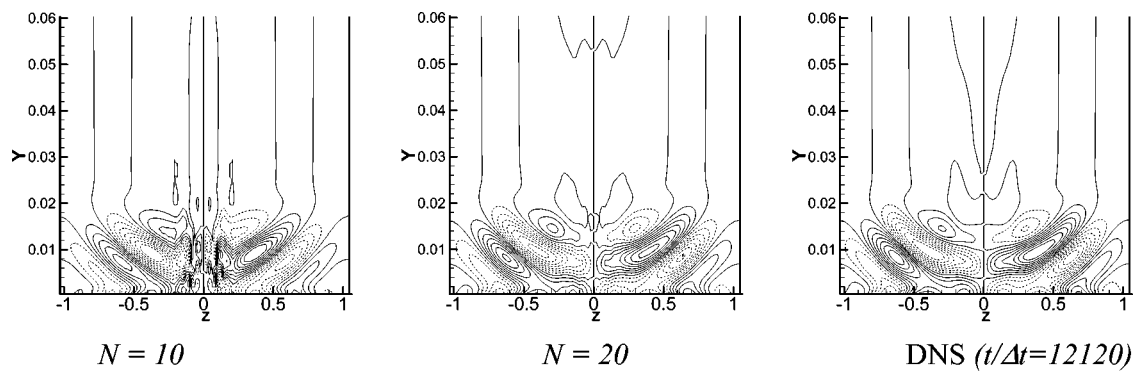
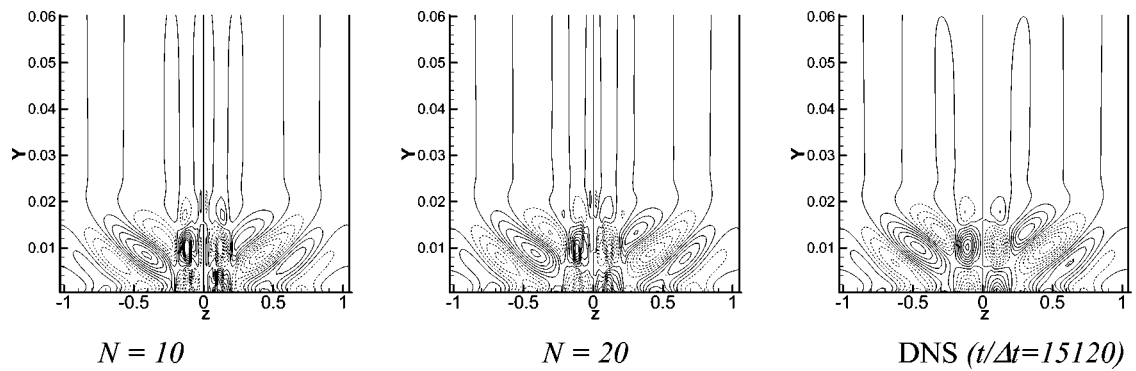


FIG. 20. Reconstruction of instantaneous ω_x of controlled flow at $t/\Delta t = 15\ 120$ via *uncontrolled* POD modes.

Figure 18 shows the rms values of ω_x for both (a) controlled and (b) uncontrolled POD bases. Again, as controlled POD



a) direct projection (i.e, DNS data belongs to the snapshot family)



b) cross projection (i.e, DNS data does not belong to the snapshot family)

FIG. 21. Reconstruction of the instantaneous ω_x via projection of POD modes. DNS data are also shown for comparison.

bases are optimal, a very accurate reconstruction is achieved with the two or four most energetic modes [see Fig. 18(a)]. Remarkably, uncontrolled POD modes can provide an accurate description of DNS data as well. This shows that on average temporal dynamics are well captured by the uncontrolled modes and appreciable differences, if any, can be expected in locations where the control is applied, i.e., locations where the rigorous changes to the flow are made.

Having compared the statistical averages via rms values, we now compare instantaneous DNS data at $x = 7.5$. Figure 19 shows a reconstruction of instantaneous ω_x via controlled

POD modes. DNS data for controlled and uncontrolled cases are also shown for comparison. As expected, very good comparison is achieved as the modes are optimal. For example, if one has to construct a low-dimensional model for uncontrolled flow, a six-equation model shall be enough. In Fig. 20, on the other hand, a controlled streamwise vorticity field is reconstructed via Eq. (10), i.e., by cross projecting the uncontrolled POD modes on the controlled data. For $N = 20$, the reconstruction is very accurate. Up to here we have essentially shown that POD modes extracted for a particular flow parameter or condition may still be used to model the

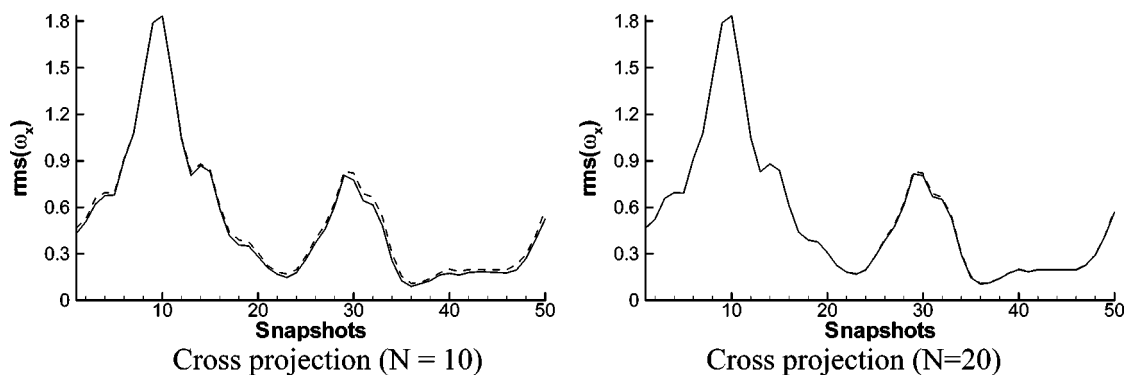


FIG. 22. Comparison of temporal rms values defined in Eq. (14). Dashed lines denote the actual DNS data, solid lines denote the reconstruction. Note that for the first 25 snapshots ($t/\Delta t = 12\ 120 - 15\ 000$) the reconstruction is via the direct projection while for the last 25 snapshots ($t/\Delta t = 15\ 120 - 18\ 000$) it is via the cross projection.

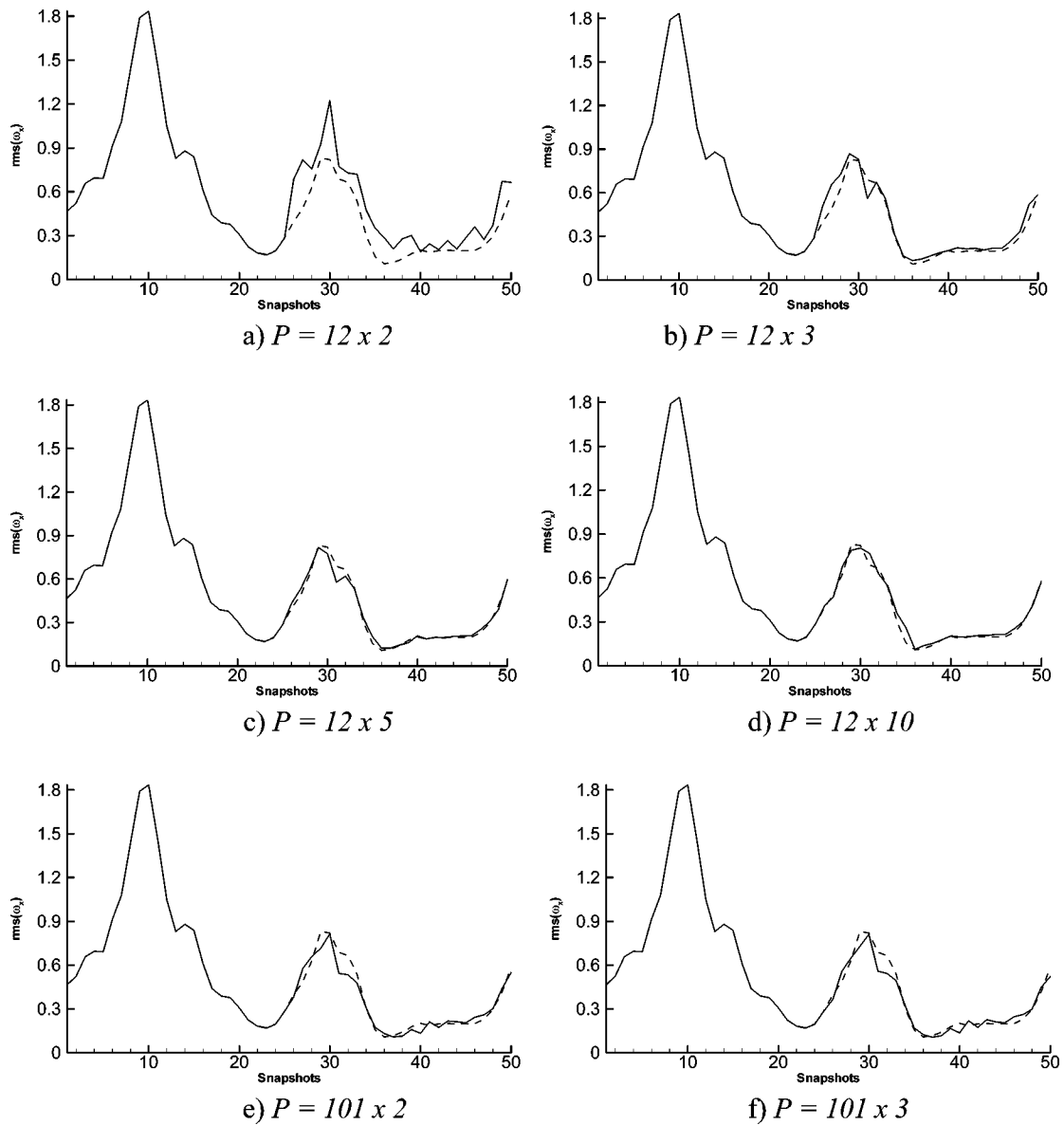


FIG. 23. Comparison of temporal rms values defined in Eq. (14). Dashed lines denote the actual DNS data, solid lines denote the reconstruction via least-squares method. Note that the total number of sensor points is $P=A \times B$ where A is the number of spanwise data points, and B is the number of wall-normal data points, i.e., $y/\Delta y=0,2,4,\dots$. The snapshots (1,2,...,50) correspond to times ($t/\Delta t=12\ 120,12\ 240,\dots,18\ 000$).

flow with different parameters or conditions by modifying the coefficients of the modes.

V. RECONSTRUCTION OF FLOW DYNAMICS VIA PREVIOUS POD MODES

In this section, we will confine ourselves to *uncontrolled* flow and investigate the possibility of reconstruction of “new” snapshots of the flow field by employing the POD modes that are extracted from “previous” or “earlier” snapshots. This investigation is important in the sense that if the flow field can be reconstructed accurately enough, an optimal control strategy can be chosen and applied efficiently with the minimal power input, for example. First of all, as in Sec. IV, the “cross projection” approach will be used in order to check the “applicability” of previous POD modes for the

reconstruction. Figure 21 shows the reconstruction of a present (unknown) snapshot via cross projection formula as

$$\omega_x^{\text{present}}(y,z,t) \cong \sum_{k=1}^N a_k^{\text{model}}(t) \Psi_k^{\text{previous}}(y,z), \quad (15)$$

$$a_k^{\text{model}}(t) = \int_{\Omega} \omega_x^{\text{present}}(y,z,t) \Psi_k^{\text{previous}}(y,z) d\Omega. \quad (16)$$

In Fig. 21, we present the DNS data as well for comparison. In addition, a comparison based on the temporal rms value defined in Eq. (14) is provided in Fig. 22. Both Figs. 21 and 22 show that the POD modes extracted from previous (or earlier) snapshots may be used to reconstruct the

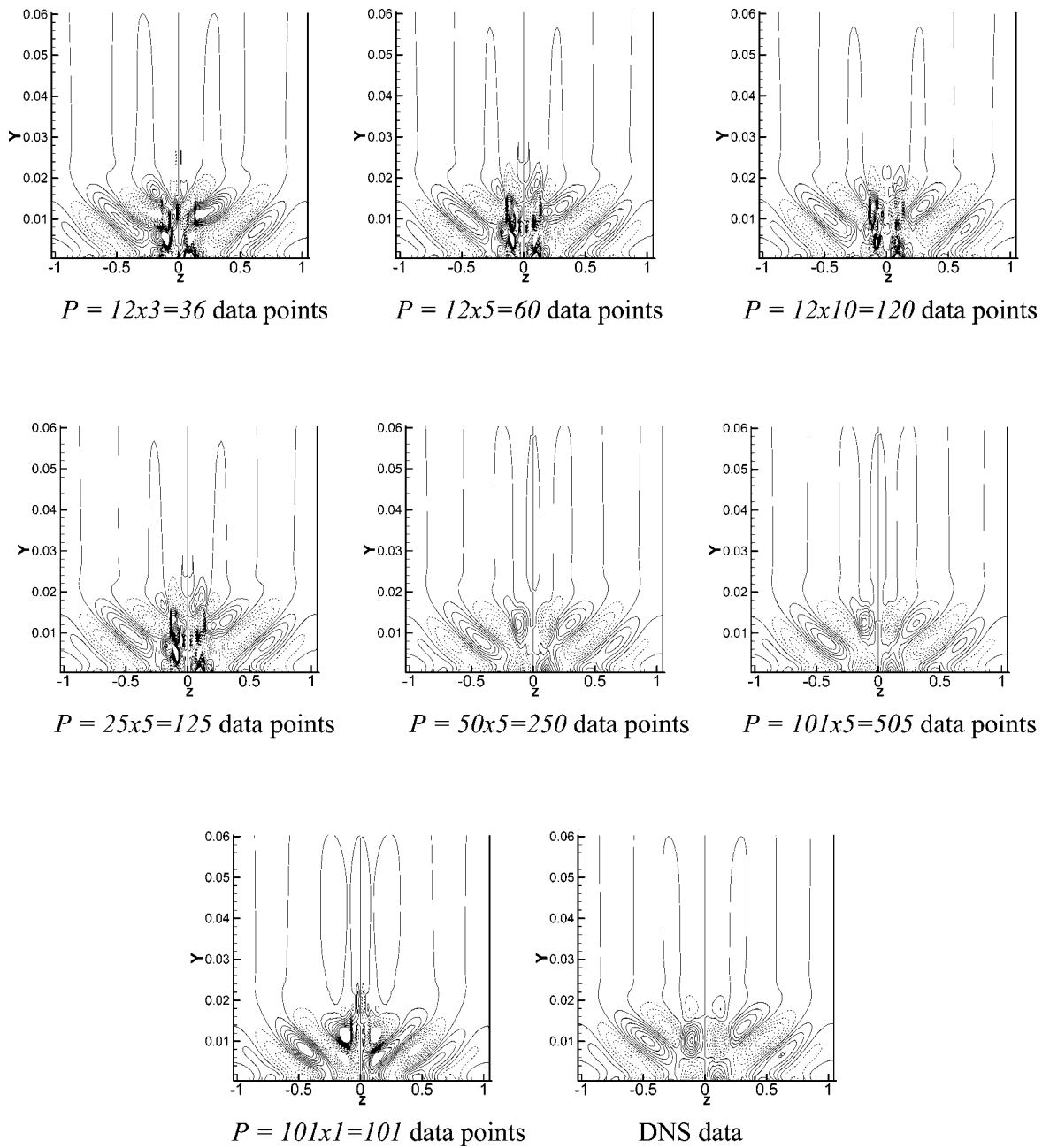


FIG. 24. Reconstruction of the instantaneous ω_x at $t/\Delta t = 15\ 120$ via least-squares projection of POD modes. DNS data are also shown for comparison.

“present” dynamics of the flow by appropriately modifying the temporal coefficients. According to Eq. (16), the cross projection approach actually requires all the present data to be known in order to calculate the temporal coefficients. Therefore, Eqs. (15) and (16) essentially represent the reconstruction of present data employing the previous POD modes. On the other hand, using POD modes, one usually needs to construct a low-dimensional model for the dynamics of temporal coefficients based on the Navier–Stokes equations and check the performance of the low-dimensional model against the cross projection formula. Low-dimensional models, then, can be used to predict the flow dynamics for later times. The construction of low-dimensional models is beyond the scope of the present paper. However, we will propose a new method in order to calculate

the temporal coefficients without the necessity of a low-dimensional model. We argue that by providing flow data only at selected locations (y_i, z_i) and employing a least-squares fit on Eq. (15), one can calculate the model coefficients without requiring the use of Eq. (16). Particularly, we can write a least-squares error as

$$E = \min \left[\sum_{k=1}^P \left\{ \left(\sum_{j=1}^N a_j \Psi_{j,k} \right) - \omega_{x,k} \right\}^2 \right] \tag{17}$$

and a least-squares fit formulation reduces to the following system of algebraic equations for the temporal coefficients:

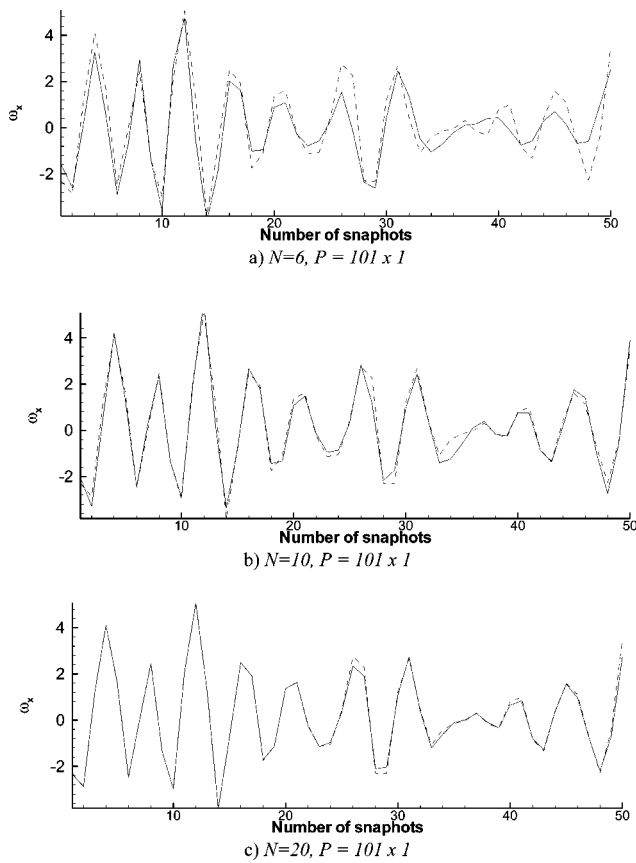


FIG. 25. Instantaneous ω_x at point ($y=0.0103, z=0.5023$) for different number of modes, N . Least-squares fit is based on $P=101 \times 1$ data points.

$$\begin{bmatrix} \sum_{k=1}^P \Psi_{1,k}^2 & \sum_{k=1}^P \Psi_{2,k} \Psi_{1,k} & \cdots & \sum_{k=1}^P \Psi_{N,k} \Psi_{1,k} \\ \sum_{k=1}^P \Psi_{1,k} \Psi_{2,k} & \sum_{k=1}^P \Psi_{2,k}^2 & \cdots & \sum_{k=1}^P \Psi_{N,k} \Psi_{2,k} \\ \cdots & \cdots & \cdots & \cdots \\ \sum_{k=1}^P \Psi_{1,k} \Psi_{N,k} & \sum_{k=1}^P \Psi_{2,k} \Psi_{N,k} & \cdots & \sum_{k=1}^P \Psi_{N,k}^2 \end{bmatrix} \times \begin{bmatrix} a_1(t) \\ a_2(t) \\ \cdots \\ a_N(t) \end{bmatrix} = \begin{bmatrix} \sum_{k=1}^P \omega_{x,k}(t) \Psi_{1,k} \\ \sum_{k=1}^P \omega_{x,k}(t) \Psi_{2,k} \\ \cdots \\ \sum_{k=1}^P \omega_{x,k}(t) \Psi_{N,k} \end{bmatrix} \quad (18)$$

In Eq. (18), P denotes the total number of data points, where $P \ll (K \times L)$ while N denotes the number of most energetic modes and determines the size of the coefficient matrix. In practice, suitable sensors can be used at various locations in the flow (usually on and near the wall) in order to measure the desired quantities. Thus, the right-hand side (RHS) of Eq. (18) can be experimentally determined in a typical application. In our case, however, we have the DNS data available

and we input the values of selected DNS data into the RHS of Eq. (18). Note that for the temporal behavior of coefficients, the coefficient matrix remains the same for a given number of modes and only the RHS column vector needs to be updated. Therefore, employing an LU decomposition, temporal coefficients can be calculated efficiently for increasing times. Figure 23 shows the temporal rms of ω_x defined in Eq. (14). Solid lines are calculated by the least-squares method described above with $N=20$, while dashed lines again denote DNS data. Figure 23 shows that by providing (measuring) as few as $P=36$ data points [Fig. 23(b)], the essential dynamical behavior of the flow for later times may be adequately reconstructed. With an increasing number of points P , a very good agreement can be obtained [see Fig. 23(d)], for $P=120$. We have to mention here that not only the number of points P taken for the least-squares fit method is important, but also the locations of these points. For example, our numerical experiments show that providing only wall data along the spanwise direction ($P=101$ in the present case), will not give an acceptable result. We find that sparse spanwise data along with near-wall data provide much better results [see Figs. 23(d) and 23(f) for comparison]. We do not claim that the locations we have chosen are optimal. However, as long as such data are accessible to sensor capabilities in a real flow, it should not be a concern. In addition, the necessity of providing enough near-wall data can possibly be transformed to measuring the gradients of the variables at the wall simultaneously. Here, we would like to point to the “vorticity flux” as reported in Ref. 29 which relies on the fact that the wall-normal vorticity gradient is related to wall-parallel gradients of the pressure, i.e., for practical purposes it should be sufficient to have a fine-enough array of pressure sensors at the wall. On the other hand, since the flow physics is present in any flow quantity one could take any sensor information for our reconstruction process, i.e., not only ω_x which we suggested.

While Fig. 23 shows the temporal behavior of spatially averaged data, in Fig. 24, we present reconstructions of instantaneous spatial distributions of ω_x data as obtained by the least-squares method. DNS data are also shown for comparison. We note that although basic flow structures are captured with the minimal number of points, considerable data points are required to capture detailed features near the symmetry plane. Figure 25 presents the instantaneous ω_x at the point ($y=0.0103, z=0.5023$) for different numbers of modes, N . It is seen that for a fixed number of data points and locations, the reconstruction is significantly improved with increasing number of modes because more information is captured from the previous snapshots. It is certain that for the robustness of the approach we require an adequate number of modes for reconstruction as seen from Fig. 25. Note that the flow dynamics beyond the 25th snapshot can be reconstructed very well here using the least-squares method with $N=20$ previously calculated POD modes. We also see from Fig. 25(c) that the reconstruction for the first 25 snapshots is virtually error-free for $N=20$ due to direct projection. On the other hand, because the values for the last 25 snapshots are calculated via the least-squares method and the

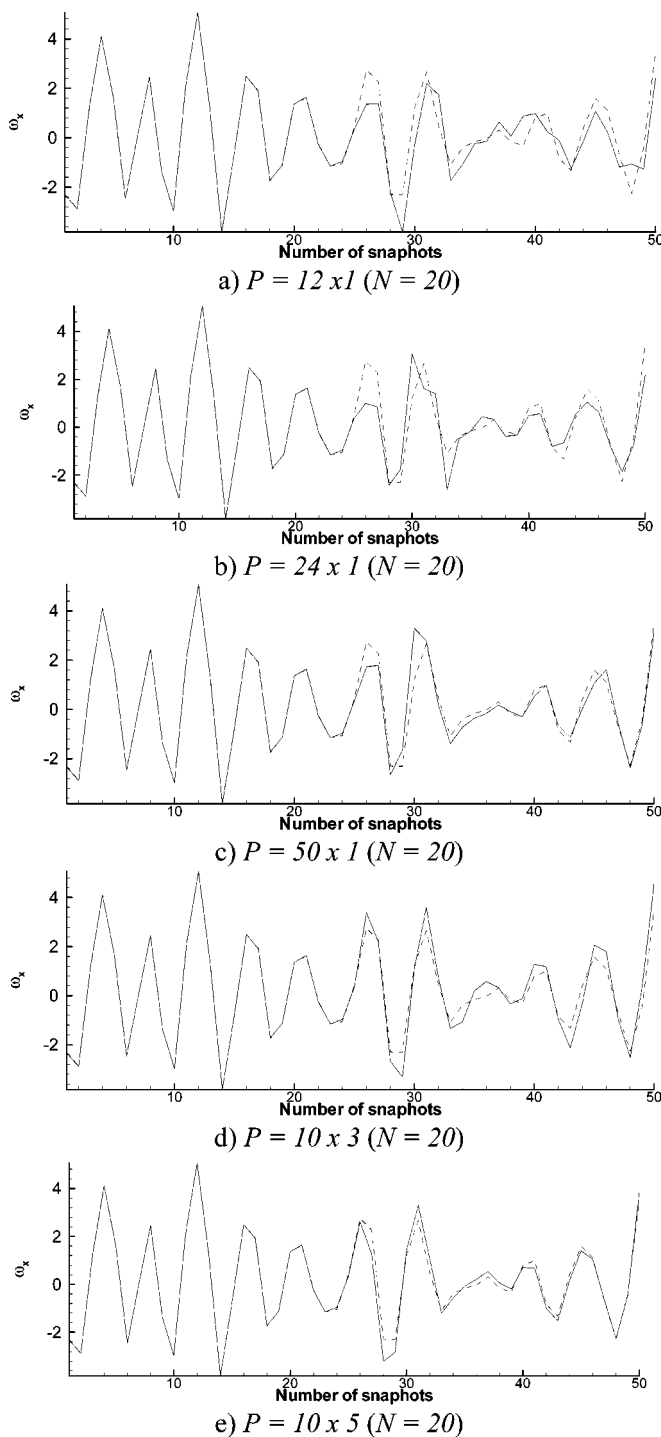


FIG. 26. Instantaneous ω_x at point ($y=0.0103$, $z=0.5023$) for different number (and location) of data points P . Least-squares fit based on $N=20$ equations (modes). Dashed lines denote the actual DNS data.

modes are not optimal for the present snapshot data, there is always a minimal error compared to the direct projection.

Finally, Fig. 26 shows instantaneous ω_x at the point ($y=0.0103$, $z=0.5023$) for different numbers (and locations) of data points, P . Here, the least-squares fit is based on $N=20$ modes. Increasing the number of sensor points and taking more points in wall-normal direction increases the accuracy of the prediction, as displayed by Fig. 26.

VI. CONCLUDING REMARKS AND OUTLOOK

In this paper, it is shown that POD modes extracted for a particular flow condition may be used to model the flow with modified conditions (through a control action, a change of Reynolds number, etc.) by modifying the coefficients of the modes. It is expected that mode coefficients have to be computed based on the modified conditions. While the cross projection approach is useful to evaluate the “suitability” of the non-optimal POD modes (i.e., whether POD modes can be used for modified conditions), it has no practical use in the reconstruction of the unknown flow dynamics as it requires the complete flow field to be known *a priori*. On the other hand, the least-squares approach introduced in this paper offers a simple and effective approach to calculate the temporal coefficients.

In practice, the method can be based on experimental data and the following outlook can be presented. Employing POD modes extracted from the upstream flow-field stations, the downstream flow field could possibly be predicted completely by utilizing sensors at a few selected downstream locations. In addition, by including the predicted snapshots into the available snapshot data, the POD modes could perhaps also be updated. With the POD modes evolving downstream, the flow field may be predicted for large downstream distances. In this way, the integration of simulation and experiment may be realized. Referred to as the “computational paradigm” by Ma *et al.*,³⁰ this approach allows simulation and experiment to work as “a symbiotic feedback” for complex flow systems. Therefore, with this approach “potential steering of the experimental measurements in real time” might become possible as envisioned by Ma *et al.*³⁰

As the most energetic POD modes for controlled and uncontrolled modes show a remarkable similarity, and unlike for turbulent flows, for transitional flows a small number of POD modes can usually capture most of the flow energy, the reconstruction method proposed here may be also used for online control tools. Such a possibility of controlling transition via low-dimensional models will be investigated in future work.

ACKNOWLEDGMENTS

H.G. gratefully acknowledges the financial support of German Academic Exchange Service (DAAD) for his visit to IAG, Universität Stuttgart which made the present work possible. The authors would also like to thank Dr. Christoph Gmelin for providing his latest DNS data.

¹J. L. Lumley, “The structure of inhomogeneous turbulent flows,” in *Atmospheric Turbulence and Radio Wave Propagation*, edited by A. M. Yaglom and V. I. Tatarski (Nauka, Moscow, 1967), p. 166.

²P. Holmes, J. L. Lumley, and G. Berkooz, *Turbulence, Coherent Structures, Dynamical Systems and Symmetry* (Cambridge University Press, Cambridge, 1996).

³G. Berkooz, P. Holmes, and J. L. Lumley, “The proper orthogonal decomposition in the analysis of turbulent flows,” *Annu. Rev. Fluid Mech.* **25**, 539 (1993).

⁴L. Sirovich, “Turbulence and the dynamics of coherent structures. I–III,” *Q. Appl. Math.* **45**, 561 (1987).

⁵D. Rempfer, “On the structure of dynamical systems describing the evo-

- lution of coherent structures in a convective boundary layer," *Phys. Fluids* **6**, 1402 (1994).
- ⁶A. Liakopoulos, P. A. Blythe, and H. Gunes, "A reduced dynamical model of convective flows in tall laterally heated cavities," *Proc. R. Soc. London, Ser. A* **453**, 663 (1997).
- ⁷C. Jing, D. Henry, H. B. Hadid, and N. Imaishi, "Low-order dynamical model for low-Prandtl number fluid flow in a laterally heated cavity," *Phys. Fluids* **15**, 2152 (2003).
- ⁸S. S. Ravindran, "A reduced-order approach for optimal control of fluids using proper orthogonal decomposition," *Int. J. Numer. Methods Fluids* **34**, 425 (2000).
- ⁹K. Afanasiev and M. Hinze, "Adaptive control of a wake flow using proper orthogonal decomposition," Technical Report No. 648/1999, Technische Universität Berlin, 1999.
- ¹⁰M. Hinze and A. Kauffmann, "Reduced order modeling and suboptimal control of a solid fuel ignition model," Technical Report No. 636/1999, Technische Universität Berlin, 1999.
- ¹¹H. M. Park, M. W. Lee, and Y. D. Jang, "An efficient computational method of boundary optimal control problems for the Burgers equation," *Comput. Methods Appl. Mech. Eng.* **166**, 289 (1998).
- ¹²J. Gerhard, M. Pastoor, R. King, B. R. Noack, A. Dillmann, M. Morzynski, and G. Tadmor, "Model-based control of vortex shedding using low-dimensional Galerkin models," AIAA Pap. 2003-4262, 33rd AIAA Fluids Conference and Exhibit.
- ¹³H. V. Ly and H. T. Tran, "Modeling and control of physical processes using proper orthogonal decomposition," *Math. Comput. Model.* **33**, 223 (2001).
- ¹⁴R. D. Prabhu, S. S. Collis, and Y. Chang, "The influence of control on proper orthogonal decomposition of wall-bounded turbulent flows," *Phys. Fluids* **13**, 520 (2001).
- ¹⁵A. Omurtag and L. Sirovich, "On low-dimensional modeling of channel turbulence," *Theor. Comput. Fluid Dyn.* **13**, 115 (1999).
- ¹⁶H. Gunes, "Low-order dynamical models of thermal convection in high-aspect ratio enclosures," *Fluid Dyn. Res.* **30**, 1 (2002).
- ¹⁷D. Rempfer, "Investigations of boundary layer transition via Galerkin projections on empirical eigenfunctions," *Phys. Fluids* **8**, 175 (1996).
- ¹⁸X. Ma, G. E. Karniadakis, H. Park, and M. Gharib, "DPIV/T-driven convective heat transfer simulation," *Int. J. Heat Mass Transfer* **45**, 3517 (2002).
- ¹⁹C. Gmelin, U. Rist, and S. Wagner, "Active control of laminar-turbulent transition using instantaneous vorticity signals at the wall," *Phys. Fluids* **13**, 513 (2001).
- ²⁰C. Gmelin, U. Rist, and S. Wagner, "Numerical investigations of active control of boundary-layer instabilities," in *Recent Results in Laminar-Turbulent Transition—Selected Numerical and Experimental Contributions from the DFG-Verbundschwerpunktprogramm "Transition" in Germany*, NNFM Vol. 86, edited by S. Wagner, M. Kloker, and U. Rist (Springer, Berlin, 2003), pp. 203–218.
- ²¹C. Gmelin, "Numerische Untersuchungen zur aktiven Dämpfung von Störungen im Vorfeld der laminar-turbulenten Transition," Dissertation, Universität Stuttgart, 2003.
- ²²F. N. Shaikh, "Investigation of transition to turbulence using white-noise excitation and local analysis techniques," *J. Fluid Mech.* **348**, 29 (1997).
- ²³U. Rist and H. Fasel, "Direct numerical simulation of controlled transition in a flat-plate boundary layer," *J. Fluid Mech.* **298**, 211 (1995).
- ²⁴M. Kloker, "A robust high-resolution split-type compact FD-scheme for spatial direct numerical simulation of boundary-layer transition," *Appl. Sci. Res.* **59**, 353 (1998), special issue, *LES and DNS of Complex Flows* (Kluwer Academic, Dordrecht, 1998).
- ²⁵M. Kloker, U. Konzelmann, and H. Fasel, "Outflow boundary conditions for spatial Navier-Stokes simulations of transitional boundary layers," *AIAA J.* **31**, 620 (1993).
- ²⁶A. E. Deane, I. G. Kevrekidis, G. E. Karniadakis, and S. A. Orszag, "Low-dimensional models for complex geometry flows: Application to grooved channels and circular cylinders," *Phys. Fluids A* **3**, 2337 (1991).
- ²⁷H. Gunes, A. Liakopoulos, and R. A. Sahan, "Low-dimensional description of oscillatory thermal convection: The small Prandtl number limit," *Theor. Comput. Fluid Dyn.* **9**, 1 (1997).
- ²⁸D. Rempfer, M. Kloker, P. Stoll, H. Bestek, and S. Wagner, "Evolution of coherent structures in flat-plate boundary layers with and without pressure gradient," *ECCOMAS 94* (Wiley, New York, 1994), pp. 478–486.
- ²⁹P. Koumoutsakos, "Vorticity flux control for a turbulent channel flow," *Phys. Fluids* **11**, 248 (1999).
- ³⁰X. Ma, G. E. Karniadakis, H. Park, and M. Gharib, "DPIV-driven flow simulation: A new computational paradigm," *Proc. Soc.* **459**, 547 (2003).